JGR Earth Surface

RESEARCH ARTICLE
10.1029/2019JF005100

Landscape Response to Lateral Advection in Convergent Orogens Over Geologic Time Scales

Paul R. Eizenhöfer[1,2], Nadine McQuarrie[1], Eitan Shelef[1], and Todd A. Ehlers[2]

[1]Department of Geology and Environmental Science, University of Pittsburgh, Pittsburgh, PA, USA, [2]Department of Geosciences, University of Tübingen, Tübingen, Germany

Key Points:
- The process of rock advection over midcrustal ramps in convergent orogens is preserved in the geomorphic record as "legacy landscape"
- Legacy landscapes are characterized by tapered topography and gradual decline in normalized channel steepness in the direction of advection
- Legacy landscapes were identified in active fold-thrust belts such as the Himalaya, Andes and Taiwan

Supporting Information:
- Supporting Information S1
- Movie S1
- Movie S2
- Movie S3

Correspondence to:
P. R. Eizenhöfer,
paul-reinhold.eizenhoefer@uni-tuebingen.de

Citation:
Eizenhöfer, P. R., McQuarrie, N., Shelef, E., & Ehlers, T. A. (2019). Landscape response to lateral advection in convergent orogens over geologic time scales. *Journal of Geophysical Research: Earth Surface*, *124*. https://doi.org/10.1029/2019JF005100

Received 9 APR 2019
Accepted 26 JUN 2019
Accepted article online 5 JUL 2019

Abstract Convergent orogens exhibit high elevations and relief, features characteristic of active rock uplift, the latter influencing normalized channel steepness (K_{sn}). In systems with significant horizontal displacement, K_{sn} values and interfluves are elevated over a region of tens of kilometers and gradually decline in the direction of rock advection. To evaluate potential relationships between elevated K_{sn}, a gradual decline in interfluve elevation (i.e., tapered topography), and lateral advection, we integrated kinematic models that simulate advection over a midcrustal ramp with a 2-D surface processes model. Varying convergence rate, bedrock erodibility, and ramp angle, we tracked topographic evolution over time. The process of advection through the region of active rock uplift above a midcrustal ramp is preserved in the geomorphic record through transient legacy landscapes characterized by (i) high-relief, advection-parallel interfluves, (ii) tapered topography, (iii) elevated and gradually declining K_{sn} values, and (iv) higher K_{sn} in trunk relative to tributary streams likely reflecting the influence of increased sediment flux, elevated interfluves, and changes in drainage area. The width of legacy landscapes provides a minimum constraint on the total lateral displacement, controlled by the duration of ramp activity and the rates of advection and erosion. The development of legacy landscapes is facilitated by spatial variations in flow convergence that occur in a 2-D setting but are not captured in idealized 1-D approaches. The presence of elevated K_{sn} and high relief, advection-parallel interfluves beyond the region of active rock uplift likely reflects the horizontal advection component inherent to convergent orogenic systems.

1. Introduction

The shape of present-day topography along convergent continental margins reflects the competition between tectonically driven displacement and erosion. At an orogen scale, fluvial erosion (Whipple, 2001; Whipple & Tucker, 1999) and both horizontal and vertical displacement along discrete fault planes (e.g., Stockmal et al., 2007; Willett et al., 2001) exert a primary control over the geomorphology of mountain ranges. Rock uplift is primarily controlled by the underlying structural geometry, whereas fluvial erosion depends on channel geometry and hydrology, material properties, erosion process, and climatic parameters such as precipitation. Fluvial channels constrain landscape relief and set the boundary conditions to which hillslope processes respond (e.g., Whipple & Tucker, 1999). Analysis of channel networks along orogens at convergent margins, where the response of surface processes to tectonic displacement plays a significant role in shaping the geomorphology, provides a valuable tool to quantify the influence of tectonic displacement and erosion on the resulting topography.

Fluvial channels systematically adjust to spatial changes in rock uplift rate by steepening or shallowing their longitudinal profile through processes of knickpoint migration and vertical incision (Crosby & Whipple, 2006; Lague et al., 2003; Rosenbloom & Anderson, 1994; Whipple & Tucker, 1999; Wobus et al., 2006). Such adjustment of channel profiles has been demonstrated, for example, across the Longmenshan Escarpment, which separates the eastern margin of the Tibetan Plateau from the Sichuan Basin (Burchfiel et al., 1995; Royden, 1997; Shen et al., 2009). This uplifted margin coincides with an abrupt decrease from high normalized channel steepness (K_{sn}) along the eastern margin of the plateau to low values in the basin (Kirby et al., 2003; Kirby & Ouimet, 2011). Similarly, the spatial distribution of K_{sn} has been shown to (i) record increases in fault throw across normal faults near the Saline Valley in eastern California (Kirby et al., 2010; Kirby & Whipple, 2012), (ii) positively correlate with differential rock uplift rates along the Mendocino triple junction in western California (Snyder et al., 2000, 2003a, 2003b) and coastal southern

California (Duvall et al., 2004), and (iii) reflect increasing rock uplift rates across an active fault-bend-fold in the Siwalik Hills in Nepal (Kirby & Whipple, 2001).

Rock uplift in convergent tectonic settings is generated through tectonic displacement over inclined fault surfaces (termed ramps and décollements for steeply or shallowly angled inclinations, respectively). In such settings, horizontal advection can be significantly higher than the resulting rock uplift rates for low angle (<45°) faults. The inclusion of a lateral advection component has been demonstrated to have a profound impact on the geomorphology at different scales. Willett et al. (2001) and Willett and Brandon (2002) have shown that at the scale of a mountain range, lateral advection shifts the location of the main drainage divide, causing a significant topographic asymmetry across it. Studying bedrock channels at a more regional scale in the Siwalik Hills of Nepal, Miller et al. (2007) predicted an asymmetry of erosion and K_{sn} across the main drainage divide when the landscape is at steady state (i.e., when the rate of erosion balances rock uplift), where the magnitude of asymmetry is dependent on bedrock erodibility and advection rate.

The relationship between rock uplift and K_{sn} has also been explored in several studies across fold-thrust belts along convergent continental margins where lateral advection rates are high and sustained over geologic time. These studies aimed to identify regions of active rock uplift and from that evaluate subsurface structural geometries and fault kinematics. For example, the distribution of elevated K_{sn} led Wobus et al. (2006) to propose out-of-sequence faulting in Central Nepal, Adams et al. (2016) to suggest active duplex growth beneath eastern Bhutan, and Yanites et al. (2010) to identify the location of active faults and/or ramp structures along the Peikang River in Taiwan. Instead of an abrupt change in K_{sn}, a gradual decrease over tens of kilometers in the direction of advection to the northwest of the Beni Escarpment in the Bolivian Andes (Gasparini & Whipple, 2014), to the southwest of the eastern Greater Caucasus (Forte et al., 2015) and to the south in Central Nepal (Whipple et al., 2016), has been interpreted as a gradual change in rock uplift rates or result of complex fault geometries over these areas. While zones of high K_{sn} within convergent orogens strongly support the presence of high rock uplift rates, they rarely show the abrupt change in K_{sn} magnitude that is characteristic for regions of high differential rock uplift rates with limited lateral advection. These zones of gradually decreasing K_{sn} potentially preserve a geomorphic record of lateral advection over a midcrustal ramp (termed "legacy landscape"). They are located within high-relief topography that gradually decreases in elevation in the direction of advection (i.e., tapered topography) and span an across-strike distance from peak to low K_{sn} values over at least ~40 km in the Bolivian Andes and Central Nepal and ~20 km in western Taiwan (Figure 1). Gradual changes in rock uplift rates along such large distances are not consistent with subsurface structures common in fold-thrust belts such as faults and ramps (Boyer & Elliott, 1982; McClay, 1992) that typically accommodate uplift over widths of ~15 km or less.

In this study we propose that lateral advection in convergent orogens can create a broad transition zone without invoking declining rock uplift rates over long distances or complex fault geometries. More specifically, we explore the role of horizontal displacement on the development of tapered topography and the gradual decrease of K_{sn} in the direction of advection as observed in convergent orogens (Forte et al., 2014, 2015; Gasparini & Whipple, 2014; Whipple et al., 2016; Wobus, Whipple, & Hodges, 2006), and whether advection over a midcrustal ramp can serve as an alternative mechanism to generate these geomorphic features. We do so through topographic analyses of natural and simulated landscapes. The simulated landscapes are produced through integrating simple structural kinematics (e.g., horizontal displacement over a midcrustal ramp in a pinned-fault and lower plate/footwall reference frame in MOVE™) with a surface processes model (CASCADE). Given the complex feedbacks in natural settings, this analysis does not intend to explore the influence of erosion on rock uplift but instead focuses on the first-order effects of lateral advection over midcrustal ramps on topography.

Our observations are in accordance with predictions made by Willett et al. (2001) and Miller et al. (2007) and show an advection-ward shift in the location of the main drainage divide and asymmetry in predicted K_{sn} values. However, because we model the midcrustal ramp with the adjacent décollement, our results show the emergence of legacy landscapes with high-relief, tapered topography composed of advection-parallel interfluves, and elevated but gradually declining K_{sn} over tens of kilometers in the direction of lateral advection over geologic time. These results are consistent with geomorphic observations in convergent orogens where lateral advection over a midcrustal ramp was proposed (e.g., McQuarrie et al., 2008; Whipple et al., 2016; Yue et al., 2005) and suggest that a complex array of fault geometries (e.g., Forte et al., 2014,

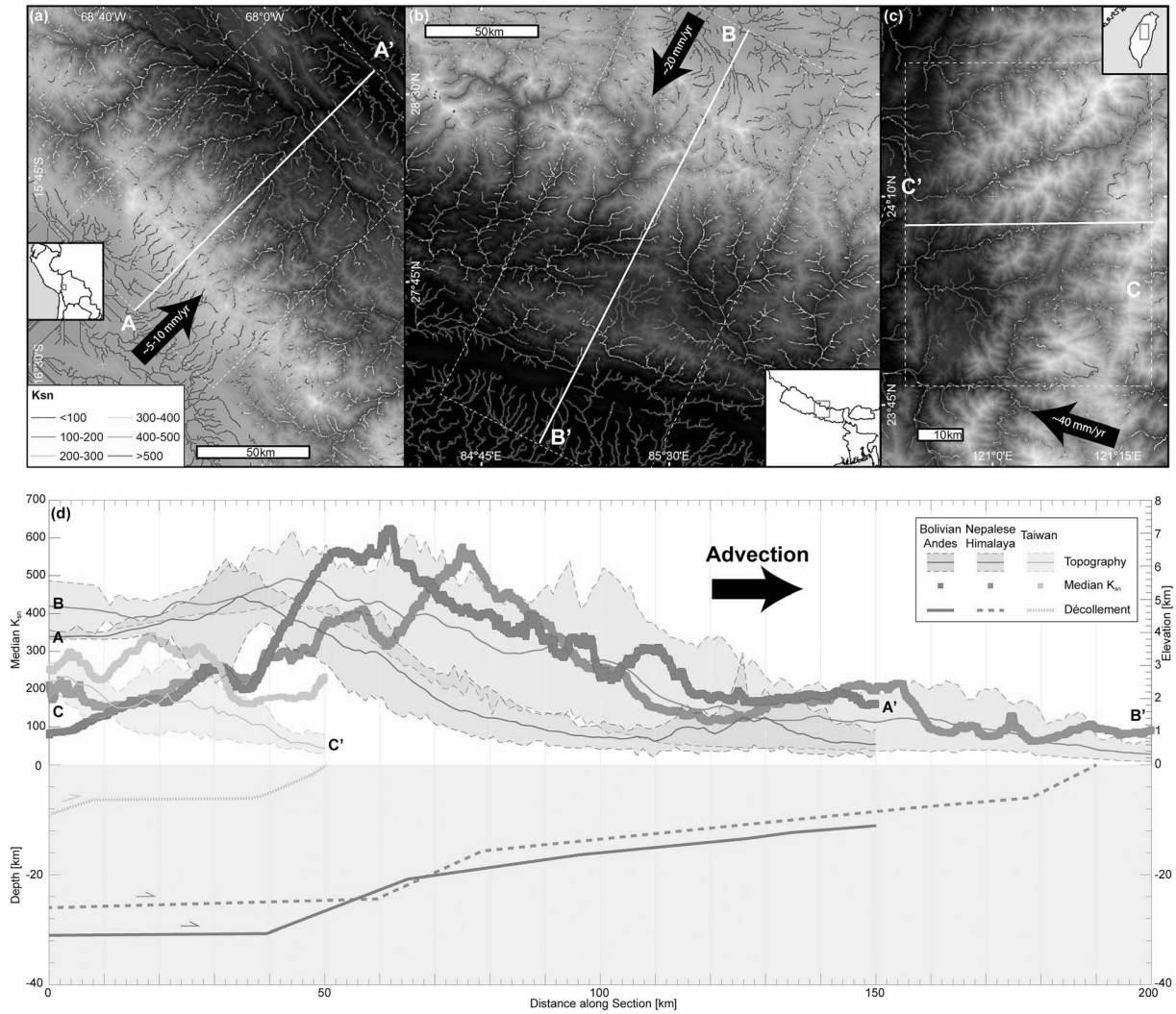

Figure 1. High-relief, tapered topography featuring advection-parallel interfluves in regions of gradually declining median K_{sn} in the direction of advection shown above proposed décollement geometries (as shown in McQuarrie et al., 2008; Whipple et al., 2016; Yue et al., 2005) using ASTER digital elevation models (~30-m resolution; U.S./Japan ASTER Science Team, 2000), K_{sn} maps of fluvial channels and swath profiles across the Beni Escarpment in the central Bolivian Andes (a, AA′), Central Nepalese Himalaya (b, BB′), and the Peikang River region of Taiwan (c, CC′). Reference concavity is $\theta_{ref} = 0.45$.

2015) or a gradual decline in rock uplift rates over large distances (e.g., Gasparini & Whipple, 2014) is not a necessity. Systematic differences in K_{sn} in trunk relative to tributary streams allude to the importance of increased sediment flux, changes in drainage area, and the transient nature of legacy landscapes. In some cases where erodibility is low relative to advection rate, migration of the main drainage divide forms a low-relief high-elevation plateau between the regions of active rock uplift and advection-parallel interfluves.

2. Theoretical Background

2.1. Prior Theoretical Work on Effects of Lateral Advection on Fluvial Channels in Bedrock

Early studies of longitudinal river profiles (Flint, 1974; Hack, 1957) revealed that rivers dynamically adjust to changes in tectonics, climate and lithology (Howard & Kerby, 1983). Tectonics in these studies was generally limited to vertical displacement. Lateral advection was not included either to keep analytical solutions simple or not considered important when applied to individual fluvial channels across a small portion of a mountain range.

Fluvial erosion into bedrock is commonly modeled through the stream power relation (e.g., Whipple & Tucker, 1999). When only vertical rock uplift is considered, changes in elevation h [L] through time t along longitudinal bedrock channel profiles have been described as follows (Howard, 1994; Howard & Kerby, 1983; Whipple & Tucker, 1999):

$$\frac{\mathrm{d}h}{\mathrm{d}t} = v_u(x) - KA(x)^m S(x)^n, \tag{1}$$

where v_u [L/t] is vertical rock uplift rate, x [L] is the position along the profile, K [$t^{-1}\,L^{1\text{-}2\mathrm{m}}$] erodibility, A[L^2] is drainage area, S [] is channel slope, and exponents m [], n [] enable nonlinear relations between erosion rate to drainage area and slope (Whipple, 2001; Whipple & Tucker, 1999). Within this framework, the slope of the bedrock channel at steady state, when the rate of channel erosion matches the rate of rock uplift ($\mathrm{d}h/\mathrm{d}t = 0$), is

$$S(x) = \left(\frac{v_u(x)}{K}\right)^{\frac{1}{n}} A(x)^{-\frac{m}{n}}. \tag{2}$$

Equation (2) guides studies that correlate differential rock uplift rates with channel steepness (i.e., the first term on the right-hand side that combines rock uplift and erodibility) along longitudinal profiles of bedrock river channels (e.g., Duvall et al., 2004; Kirby & Whipple, 2001, 2012; Snyder et al., 2000). The concavity m/n empirically ranges between 0.35 and 0.6 and reflects the dominant mechanical process of fluvial erosion as well as the relationship between channel geometry, discharge, and drainage area (Whipple et al., 2000; Whipple & Tucker, 1999). Assuming a regionally constant channel concavity (i.e., m/n) this relation is utilized to derive the normalized channel steepness (K_{sn}) for a region.

In the analysis of orogen topography, lateral advection is typically considered negligible for regions where the ratio between horizontal and vertical displacement is small. However, a lateral advection component that is higher or comparable in magnitude to rock uplift, as typically occurs along convergent continental margins and fold-thrust belts (e.g., Andes, Himalaya, Zagros, Caucasus, Taiwan, Timor), meaningfully influences the relations in equation (1):

$$\frac{\mathrm{d}h}{\mathrm{d}t} = v_u(x) - v_h(x)\frac{\mathrm{d}h}{\mathrm{d}x} - KA(x)^m S(x)^n, \tag{3}$$

where v_h [L/t] represents the lateral advection rate (e.g., Miller et al., 2007; Willett et al., 2001). For $v_{\mathrm{h}}(x) \neq 0$, K_{sn} and channel concavity become asymmetric (Willett et al., 2001), and fluvial channels develop non-typical slope-area relations across the main drainage divide (i.e., channel slopes will diverge from linearity in log-log space as a function of drainage area; Miller et al., 2007).

A nondimensionalized parameterization of equation (3) with $h^* = h/LS$, $t^* = tv_0/LS$, $x^* = x/LS$, $A^* = A/A_0$, and advection over a ramp described as $v_{\mathrm{h}} = v_0\cos(\alpha)$, $v_{\mathrm{u}} = v_{\mathrm{r}} + v_0\sin(\alpha)$ for $v_0 \neq 0$ (v_0 [L/t], advection rate; v_{r} [L/t], regional rock uplift rate; α [rad], ramp angle; Figure 2) reveals a direct trade-off between advection rate v_0 and erodibility K (for some reference area A_0), commonly described as fluvial efficacy number ε (e.g., Miller et al., 2007; Willett et al., 2001):

$$\frac{\mathrm{d}h^*}{\mathrm{d}t^*} = \frac{v_r}{v_0} + \sin(\alpha) - S\cos(\alpha) - \epsilon A^{*m} S^n \text{ with} \tag{4a}$$

$$\epsilon = \frac{KA_0^m}{v_0}. \tag{4b}$$

Equations (3), (4a) and (4b) yield two end-member states for the behavior of fluvial channels that undergo advection over a ramp (Figure 2). Assuming $n = 1$, for $KA^{\mathrm{m}} \gg v_0$ (large ε) an asymmetric drainage divide will develop and reach steady state (*type 1*; Miller et al., 2007; Willett et al., 2001), whereas, for example, for $K = 0$(small ε), the elevated topography formed in the region of active rock uplift will be translated in the direction of advection, forming an elevated plateau that never reaches steady state (*type 2*). This simplified view based on a detachment-limited stream power erosion model does not take into account the lateral

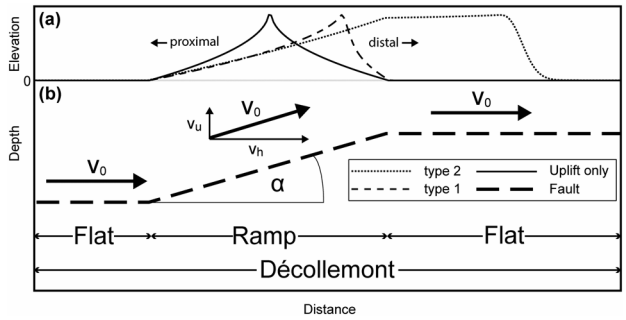

Figure 2. Simplified relations between fault geometry (b) and the development of *type 1* (asymmetric drainage divide and steady state reached) and *type 2* (runaway fluvial channel profile without reaching steady state) end-member topographic responses (a) following the stream power relation in equations (3) and (4). v_0: convergence rate; v_h: horizontal advection component; v_u: rock uplift component; and α: ramp angle.

variability in flow direction of channels with respect to the direction of advection over a ramp, hillslope processes, or interactions between hillslope and fluvial processes; all of which have the potential to influence the shape of fluvial channels in natural examples. Two-dimensional landscapes with spatial variations in flow directions (and hence drainage area) are expected to produce lateral variations in ε that will form a combination and/or range of *type 1* and *type 2* fluvial responses.

2.2. Landscape Response Time

Processes of lateral advection and fluvial channel erosion are associated with characteristic time scales that influence the topographic response to tectonic changes. Lateral advection of topography over a ramp (Figures 2 and S5; Elliott et al., 2016; Hubbard et al., 2016; McQuarrie et al., 2008; Tate et al., 2015; Whipple et al., 2016; Yue et al., 2005) can be viewed as portions of a landscape that experience a transient episode of high rock uplift. Fluvial channels in bedrock respond to tectonic or climatic perturbations through processes such as upstream knickpoint migration where the knickpoint velocity (v_{KP} $[L/t]$) is derived from equation (1) (Crosby & Whipple, 2006; Rosenbloom & Anderson, 1994; Whipple & Tucker, 1999):

$$v_{KP} = KA^m S^{n-1} \tag{5}$$

Equation (5) generally implies that (for $n = 1$) erodibility K and drainage area A determine how fast a fluvial channel translates perturbations upstream and regains equilibrium. Everything else being equal, river systems with large drainage area (e.g., trunk streams) are expected to communicate perturbations faster compared to those of smaller drainage area (e.g., tributary streams; Rosenbloom & Anderson, 1994; Tucker & Whipple, 2002; Weissel & Seidl, 1998), which is consistent with empirical observations (Berlin & Anderson, 2007; Crosby & Whipple, 2006; Shelef et al., 2018). However, this fluvial response also depends on the location of the individual channel within its drainage network (Perron & Royden, 2013; Royden & Perron, 2013; Willett et al., 2014). In a 2-D landscape a tributary stream downstream in the drainage network will respond faster than a tributary stream with the same drainage area upstream.

The fluvial channel response to tectonic perturbations is subsequently radiated to neighboring hillslopes by resetting their fluvial base level (e.g., Fernandes & Dietrich, 1997). The time scale of hillslope response varies with the hillslope topography and soil transport process and can range from abrupt response in the case of steep topography where soil transport is dominated by landslides (e.g., Moon et al., 2015, and references therein) to a gradual response in the case of gentle hillslopes where soil transport is dominated by processes of soil diffusion (e.g., Culling, 1960; Hurst et al. 2012).

2.3. CASCADE

CASCADE (Braun et al., 1999; Braun & Sambridge, 1997) was chosen to model long-term landscape evolution because of its ability to integrate vertical and horizontal displacement trajectories based on fault geometries modeled in MOVE™ (added in this study) and its capability to simulate surface processes at mountain range scales. CASCADE combines transport- and detachment-limited fluvial regimes by assuming that changes in elevation along fluvial channels are governed by erosion-deposition length scales $l_f[m]$ and sediment flux Q_f $[L^3/t]$ relative to the equilibrium stream carrying capacity Q_f^{eqb} $[L^3/t]$ (Braun et al., 1999; Kooi & Beaumont, 1994):

$$\frac{dh}{dt} = -\frac{1}{l_f w}\left(Q_f^{eqb} - Q_f\right) \text{ with} \tag{6a}$$

$$Q_f^{eqb} = -K_f Q_w S, \tag{6b}$$

with Q_w $[L^3/t]$ representing river discharge as a product of drainage area and precipitation rate (uniform in this study), w $[L]$ is channel width as a function of discharge, and K_f [] is a transport coefficient. Detachment-limited conditions occur where $Q_f \ll Q_f^{eqb}$ In that case, describing Q_f^{eqb}as a function of drainage area

produces the commonly used stream power relation with $m = 0.5$ and $n = 1$ (see Text S1 in the supporting information). We set the model to distinguish between alluvial cover (l_f = 100 m; Table 2) and bedrock (l_f = 1,000 m; Table 2), where the latter is less erodible, keeping K_f the same in equations (6a) and (6b) in each model run. Sediment flux (including material derived from hillslope processes) and the stream carrying capacity are tracked over the modeled landscape to determine whether sedimentation or erosion occurs (e.g., streams operating at sediment capacity, $Q_f \geq Q_f^{eqb}$, will deposit sediment). Thus, CASCADE tracks if fluvial incision is occurring in bedrock or alluvial material, or if local deposition is taking place. Hillslope processes are modeled using a linear diffusion model ($K_d = 2.0 \times 10^{-6}$ km^2/year in all models; Table 2) that includes a land sliding component with a threshold hillslope angle (30° in all models).

3. Model Setup and Topographic Analytical Approach

3.1. MOVE ™/CASCADE Integration

To explore the effects of lateral advection on the evolution of topography and K_{sn} values over geologic time, we conducted a suite of numerical experiments that couple a landscape evolution (CASCADE) and kinematic model of lateral advection over a flat-ramp-flat structure that is spatially fixed in a lower plate (footwall) reference frame (MOVE™; Figure 3). We used a version of CASCADE (Braun et al., 1999; Braun & Sambridge, 1997) that was rewritten in FORTRAN 90 which includes modifications to file input/output, precipitation (Yanites & Ehlers, 2012, 2016), and specified kinematics (added in this study). Our integrated models explicitly include a vectoral displacement trajectory that results from the combination of horizontal and vertical advection components. The trajectories were derived by modeling the kinematics above simple flat-ramp-flat subsurface geometries (Figure 3) using a fault-parallel flow algorithm (Egan et al., 1997; Kane et al., 1997; Ziesch et al., 2014) in MOVE™. Our calculation of surface and subsurface displacements with MOVE™ follows the workflow of McQuarrie and Ehlers (2015, 2017) with the exception that we do not calculate thermochronometer cooling ages in this study.

The CASCADE model domain spans a width of 60 km along the y axis and a length of 200 km along the x axis parallel to the direction of advection with an initial average node spacing of ~0.5 km. At the start of each model the décollement is located at a depth of ~−8 km at $x = 0$ km, reaches a depth of ~−10 km at $x = 50$ km, where it steps down along a steeper midcrustal ramp, and ultimately descends to a depth of ~−21 km at $x = 150$ km corresponding to a décollement dip angle of 2° (Figures 3a and 3b). Such modeled fault geometries, especially the spatial extents of midcrustal and/or basement ramps, are common features in fold-thrust belts (Allmendinger & Zapata, 2000; Bollinger et al., 2006; Boyer & Elliott, 1982; Kley, 1996; McQuarrie et al., 2008; Pandey et al., 1995; Rak et al., 2017; Tate et al., 2015; Whipple et al., 2016; Yue et al., 2005). Although fold-thrust belts typically evolve by the systematic activation and propagation of multiple faults and ramps, activity on a single ramp may exists for 2–15 Myr (e.g., Hubbard et al., 2016; Long et al., 2012; Rak et al., 2017; Tate et al., 2015).

Advection trajectories were extracted from MOVE™ after incremental steps of d_{incr} = 10 km (Figure 3b; see Figure S2 for d_{incr} = 1 km) including isostatic responses (Table 1). Rock uplift rates generated above the flat décollement represent ~3% of the total convergence rate and thus have a negligible influence on the simulated landscapes. Lateral advection rates decrease where rock uplift rates are high and vice versa in accordance with the ramp geometry (e.g., equation (4a)).

The resulting displacement trajectories are assigned to each surface node in the CASCADE triangulated irregular network (TIN). TIN nodes then physically move according to their prescribed vector. Updates on trajectory assignments and dynamic remeshing based on individual node distances and TIN triangle mesh surface areas are performed regularly in 2500 model year intervals to avoid any potential node overlapping, especially at higher advection rates.

We evaluated changes in advection rates v_0, ramp angles α_r and erodibility K (see Text S1 for conversion from K_f and other CASCADE input parameters to K) to assess the effect that a range of realistic parameters (see for comparison Yanites & Ehlers, 2012, 2016) exert on the evolution of topography and K_{sn} at the mountain range scale. Changes in ramp angle were performed without changing the depth of the décollement, leading to variable ramp widths but keeping the elevation of the top of the ramp fixed. For simplicity, erodibility K is spatially uniform in each model run. All other parameters (e.g., diffusivity K_d, erosion-deposition length

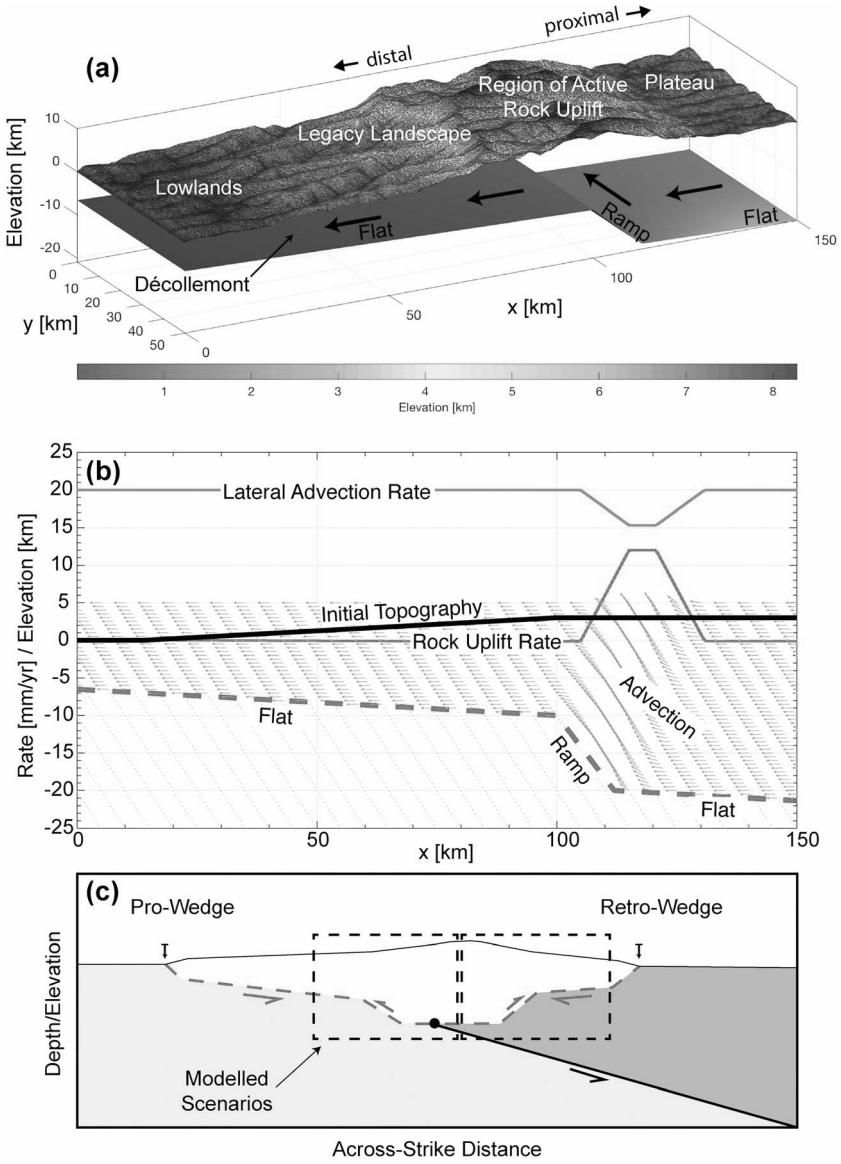

Figure 3. (a) Illustration of topography translated over the décollement, and definition of landscape components used in this study. (b) Profile view along the *x* axis of the kinematic model setup (black line: idealized tapered topography prior to initial river incision and lateral advection; red dashed line: décollement; vertically exaggerated). (c) Applicability of model setup within a double-wedge orogenic framework assuming regions of active uplift are created through advection over discrete midcrustal ramps.

scales l_f, and river bed width proportionality constant a, see also Text S1) are the same for all model runs (Table 2). This experimental setup facilitates a direct comparison to and a better understanding of measured geomorphic signals in natural examples such as the Andes, Himalaya, or Taiwan.

The initial conditions for all CASCADE and MOVE™ models are an idealized tapered topography with an average topographic slope angle of $\alpha_t = 2°$ reaching maximum elevations of $h = 3$ km at $y \approx 100$ km (Figure 3b) which then remains constant. In CASCADE we then produced a more natural landscape by simulating fluvial incision and hillslope processes without lateral advection or rock uplift for $t_{init} = 0.5$ Myr (subsequently termed "initial topography"; see Figure S3 for $t_{init} = 0.25$ Myr), after which advection was turned on. This more natural initial topography (at $t = 0$ Ma after t_{init}) may vary in detail (e.g., channel orientation and distribution) across individual models.

Table 1
Summary of MOVE™ Model Parameters

Model	α_r (deg)	α_d (deg)	d_{incr} (km)	Isostasy	d_{total} (km)	v_0 (mm/a)	t_{total} (Ma)
M10a	40	2	10	ρ = 2,650 m^3/kg	50	10	5
M10b							
M10c	20						
M10d	60			EET = 70 km			
M10e	40			$\alpha_t = 2°$			
M10f			1				
M20a	40	2	10	(as above)	100	20	5
M20b							
M20c	40/40/40						
M0	40	2	0	(as above)	0	0	5
M5	40	2	10	(as above)	25	5	5
M40	40	2	10	(as above)	100	40	2.5

Note. α_r: ramp angle; α_d: décollement angle; d_{incr}: displacement for each deformation step; ρ: average crustal density; EET: effective elastic thickness, α_t: average topographic taper angle; d_{total}: total amount of displacement; v_0: convergence rate; t_{total}: total model run time.

Boundary nodes along $y = 0$ and $y = y_{max}$ move vertically and horizontally, whereas boundary nodes along $x = x_{max}$ are free to move vertically if rock uplift is present. Along $x = 0$ boundary nodes are fixed at zero elevation. Furthermore, boundary nodes are open to sediment flux. All models and their parameters are listed in Tables 1 and 2.

3.2. Topographic Analysis

Topographic analyses of simulated topography and of digital elevation models (DEMs) of natural landscapes were performed using the MATLAB® program TopoToolbox v2 (Schwanghart & Kuhn, 2010; Schwanghart & Scherler, 2014). Values for K_{sn} were extracted from fluvial channels with a minimum upstream drainage area of $A_{min} = 20\ km^2$ and $A_{min} = 10\ km^2$ to exclude hillslope diffusion effects adopting a reference concavity of $\theta_{ref} = 0.5$ and $\theta_{ref} = 0.45$ for simulated topography and natural landscapes, respectively. $\theta_{ref} = 0.5$ is inherent to CASCADE (Text S1), while $\theta_{ref} = 0.45$ provides the best fit to natural landscapes (Gasparini & Whipple, 2014; Kirby & Whipple, 2012). Using different θ_{ref} between natural and modeled landscapes does not meaningfully limit our analyses because our focus is on the spatial distribution of K_{sn}, not its magnitude. Topographic data of natural landscapes were retrieved from ASTER DEMs at a resolution of ~30 m (U.S./

Table 2
Summary of CASCADE Model Parameters

Model	Width/length (km)	R (km/node)	K_t	K_t (km^2/a)	a [(a/m)$^{0.5}$]	b (m/a)	ll_f (m)	t_{init} (Ma)	t_{total} (Ma)
M10a	60/200	~0.5	3.5×10^{-4}	2.0×10^{-6}	0.1	0.6	1,000 (bedrock)	0.5	5
M10b			1.75×10^{-4}						
M10c			3.5×10^{-4}				100 (alluvial)		
M10d									
M10e								0.25	4.8
M10f								0.5	5
M20a	60/200	~0.5	3.5×10^{-4}	2.0×10^{-6}	0.1	0.6	1,000/100	0.5	5
M20b			7.0×10^{-4}						
M20c			3.5×10^{-4}						
M0	60/200	~0.5	3.5×10^{-4}	2.0×10^{-6}	0.1	0.6	1,000/100	0.5	5
M5	60/200	~0.5	3.5×10^{-4}	2.0×10^{-6}	0.1	0.6	1,000/100	0.5	5
M40	60/250	~0.5	3.5×10^{-4}	2.0×10^{-6}	0.1	0.6	1,000/100	0.5	3

Note. Width/length: model domain; R: initial model resolution; K_f: fluvial transport coefficient; K_d: diffusivity constant; a: channel width proportionality constant; b: precipitation; l_f: erosion/deposition length scale; t_{init}: initial fluvial incision time prior to tectonic advection; t_{total}: total model run time.

ASTER Science Team, 2000). TINs of simulated landscapes were converted to regularly gridded DEMs with a resolution of 0.5 km of which a width of 50 km and length of 150 km of the model domain were analyzed to minimize boundary effects. We utilize summary statistics (e.g., mean and median; Figure 1d) over swaths to characterize the topography along a profile. As a result, these swath profiles may be prone to effects of local depressions, a varying density of differently sized rivers, or local knickpoints leading to local variabilities in K_{sn}. In CASCADE the filling of topographic depressions is governed by depositional processes and hence depressions may not always be filled. Statistical artefacts may be more pronounced when separating between trunk and tributary streams because of the low number of channels within each swath given the limited model domain.

4. Model Results

4.1. Initial Topography

The initial topography for all models at $t = 0$ Ma reflects an idealized tapered topography with a more natural landscape (e.g., Figures 4 and 5 at $t = 0$ Ma) and shows a generally uniform distribution of very low K_{sn} (<500) across the surface. Slope parallel rivers developed where the initial topography was inclined ($x \approx$ 0–100 km; see also Figure 3b), whereas more randomly oriented rivers emerged on the plateau region ($x \approx$ 100–150 km). The transition zone between these two regions contains some channels oriented approximately perpendicular to the dip direction of the tapered topography, which can be used to track the magnitude of lateral advection over time (e.g., arrows in Figures 4 and 5).

4.2. Topographic Evolution Over Time

Comparison of two models with different advection rates v_0 reveals the development of two distinct types of modeled landscapes over time. The initiation of lateral advection leads to a visible increase in elevation and K_{sn} (>1,000) above the region of active rock uplift at 0.5 Ma independent from advection rate and lateral displacement (Figures 4 and 5 at 0.5 Ma; models *M10a* and *M20a* with $v_0 = 10$ mm/year and $v_0 = 20$ mm/year after 5 km and 10 km of total displacement, respectively). The distribution of high K_{sn} reflects the imposed rock uplift field (Figure 3b) but also shows a K_{sn} versus distance pattern that is asymmetric with steeper slopes and higher values in the direction of advection. On the distal lowlands and proximal plateau (Figure 3a), where vertical displacement is negligible, K_{sn} decreases and there is no elevation gain. The higher advection rate facilitates a more rapid formation of the main drainage divide that separates the plateau from the lowlands above the region of active uplift perpendicular to the direction of advection compared to the slower rate.

After 1.5 Myr (Figures 4 and 5 at 1.5 Ma), a well-defined high elevation main drainage divide (at $x \approx 105$ km and $x \approx 115$ km, respectively) forms. In both models ($v_0 = 10$ mm/year and $v_0 = 20$ mm/year) the divides are asymmetric with respect to the region of active rock uplift and are shifted in the direction of advection in accordance with the prescribed rates and clearly separate the plateau region from the lowlands. River systems on the plateau ($x > 130$ km) maintain their nonuniform orientation, whereas river systems toward the lowland ($x < 80$ km and $x < 90$ km for the lower and higher advection rates, respectively) remain advection parallel. River systems in the immediate vicinity of the main drainage divide, however, respond to the new conditions by becoming quasi-perpendicular to the divide, independent from their orientation before the formation of the main drainage divide. On the plateau region and the lowlands, not including rivers immediately adjacent to the main drainage divide, fluvial channels still largely follow their original configuration but are displaced by ~15 and ~30 km, respectively, corresponding to the prescribed advection rates (arrows in Figures 4 and 5). The highest K_{sn} (>1,000) occurs within the region of active rock uplift, but their distribution across the main drainage divide shows notable variations in magnitude (here and in all subsequent time steps): channels advected toward the divide (termed proximal streams; Figures 2 and 3) show a pronounced increase in K_{sn} over the uplift field and then lower their K_{sn} as they approach the divide, whereas channels advected away from the divide (termed distal streams; Figures 2 and 3) show very high K_{sn}. Away from the main drainage divide in the direction of advection, both models show a region of migrated advection-parallel interfluves accompanied by elevated K_{sn} relative to background values, ~10 and 20 km away from the region of active rock uplift, respectively. These regions are subsequently referred to as "legacy landscapes" (see Figure 3a and shaded areas in Figures 4 and 5 at $t = 4.5$ Ma).

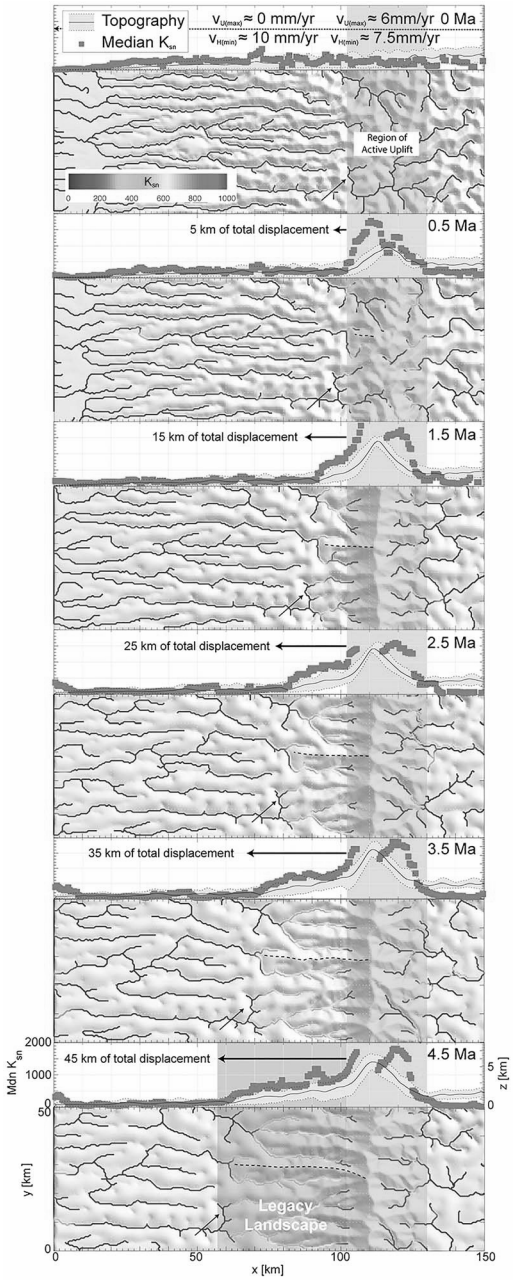

Figure 4. Simulated landscapes showing the evolution of topography and K_{sn} through time featuring the emergence of a legacy landscape (shaded area at 4.5 Ma) with fixed main drainage divide perpendicular to the direction of advection in map and cross-section views with an advection rate of v_0 = 10 mm/year (model *M10a*, Tables 1 and 2) from model time t = 0 Ma to t = 4.5 Ma in steps of 1 Myr. Dashed lines in map views mark evolution of a single advection-parallel interfluve, and arrows in map view highlight horizontal displacement of a distinct geomorphic marker. Red vertical bar outlines region of active rock uplift. Here and in all subsequent model and natural DEMs: K_{sn} in (1) map view were smoothed over a five-node average filter, whereas in (2) cross-section view values were binned and then smoothed over a 5-km moving window; increased K_{sn} near the model edge at x = 0 are model artefacts that result from the advection of topography with potentially higher elevation than the fixed boundary nodes. Mdn K_{sn}: median K_{sn}, $v_{u(max)}$: maximum vertical advection rate, and $v_{h(min)}$: minimum horizontal advection rate (see also Figure 3). See also Movie S1.

The model topography at 2.5 Ma significantly differs with respect to advection rate and the appearance of the legacy landscape (all other model parameters being equal). For lower advection rates (Figure 4 at 2.5 Ma) the location of the main drainage divide remains spatially fixed at $x \approx$ 110 km, whereas for the higher rate the divide migrates in the direction of advection (Figure 5 at 2.5 Ma). For lower advection rates (Figure 4), high-elevation advection-parallel interfluves elongate as they are advected away from the region of active rock uplift according to the total displacement (dashed lines in Figure 4) defined by the prescribed advection rate. New tributary streams form along the slopes of the interfluves at high angle to their respective trunk streams (e.g., the central trunk stream right after leaving the region of active rock uplift below the dashed line from time step 1.5 to 2.5 Ma in Figure 4). For higher advection rates, an initial elongation of advection-parallel interfluves is followed by the migration of the main drainage divide away from the region of active rock uplift, and the formation of an elevated low-relief plateau between the advected divide and the region of active rock uplift.

For lower advection rates, at t = 4.5 Ma, ~45 km of the landscape has been advected over the midcrustal ramp (Figure 4 at t = 4.5 Ma). The across-strike K_{sn} distribution shows a migration of elevated values (<1,000) that decrease in the direction of advection away from the region of active rock uplift. Highest values (>1,000) are always present within the region of active rock uplift. The width of the legacy landscape is approximately equivalent to the total displacement of 45 km prescribed to the model. At higher advection rates (Figure 5 at t = 4.5 Ma) ~90 km of the landscape has been advected through the region of active uplift. Notably, the main drainage divide has migrated ~30 km. The drainage divide separates a low-relief landscape (~30-km wide) from the advection-parallel interfluves. The former is characterized by low K_{sn} (<500) and the latter by elevated K_{sn} values, which decrease in magnitude from the main drainage in the direction of advection. The spatial extent of the legacy landscape at higher advection rates approximates the prescribed total displacement of 90 km. For both scenarios the region of active rock uplift is still marked by highest K_{sn}. However, with high advection rates and sufficient amount of time for advection of the drainage divide, the highest values are found in proximal streams.

Regions that experience negligible rock uplift (i.e., the lowlands and the plateau that is moving into the region of active rock uplift) are identified by their low local relief indicative of the prolonged influence of continued erosion through fluvial and hillslope processes at all time steps.

4.3. Effect of Advection Rate

The behavior of the drainage divide and maximum width of legacy landscapes, and thus K_{sn} beyond the region of active rock uplift, show a systematic sensitivity to changes in advection rates. Without a horizontal advection component (Figure 6, "No Advection"; model *M0*; see also Movie S3) a fixed and symmetric main drainage divide develops at $x \approx$ 118 km within the region of active rock uplift after 2 Myr. This divide is slightly shifted toward the plateau region due

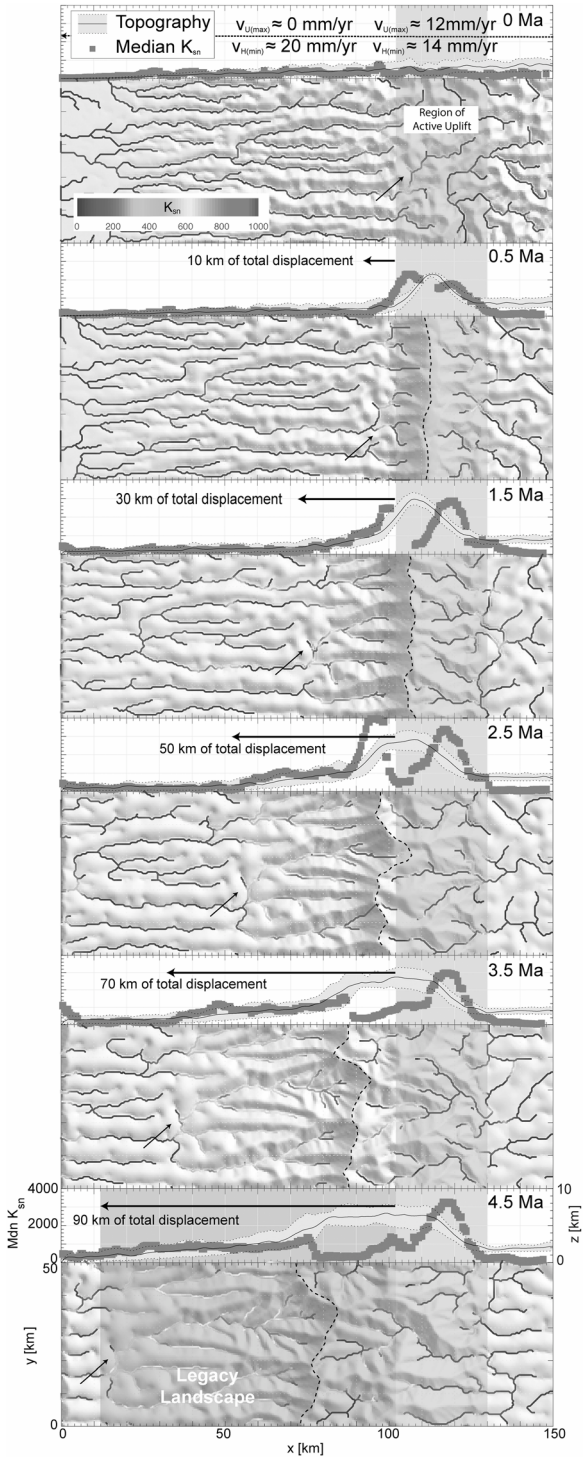

Figure 5. Simulated landscapes showing the evolution of topography and K_{sn} through time featuring the emergence of a legacy landscape (shaded area at 4.5 Ma) with migrated main drainage divide in map and cross-section views with an advection rate of $v_0 = 20$ mm/year (model *M20a*, Tables 1 and 2) from model time $t = 0$ Ma to $t = 4.5$ Ma in steps of 1 Myr. Dashed line in map view delineates location of the main drainage divide, and arrows in map view highlight horizontal displacement of a distinct geomorphic marker. Shaded red vertical bar outlines region of active rock uplift. Mdn K_{sn}: median K_{sn}. See also Movie S2.

to the base level difference of ~3 km between the hinterland plateau and the lowlands. As expected, the distribution of K_{sn} corresponds to the prescribed rock uplift field (i.e., equation (2)), and does not show the drop in K_{sn} across the main drainage divide that develops when a horizontal advection component is present (Figures 4–6). In the absence of horizontal advection, a topographic steady-state (i.e., Willett & Brandon, 2002) is reached without the emergence of a legacy landscape.

In models that include lateral advection, the location of the main drainage divide shifts in the direction of advection. For low convergence rates ($v_0 <$ 20 mm/year, Figure 6; models *M5* and *M10a*), the asymmetric main drainage divide is fixed above the region of active rock uplift. The location of highest K_{sn} slightly shifts in the same direction. Proximal streams show elevated K_{sn} above the ramp and decreasing K_{sn} toward the divide as described earlier. In contrast, high convergence rates ($v_0 \geq 20$ mm/year) lead to a migration of the main drainage divide, located at $x \approx 66$ km (model *M20a*) and $x \approx 104$ km (model *M40*) after 2 Myr. The distribution of K_{sn} across the legacy landscapes is the same as described in the previous section with highest K_{sn} above the region of active rock uplift and elevated K_{sn} values that decrease in the direction of advection. For the high advection rates, an uplifted low-relief (low K_{sn}) plateau forms behind the advected drainage divide. Independent of advection rate, the extent of the legacy landscapes is the same as the total amount of displacement (Figures 4–6).

4.4. Effect of Erodibility

Comparison of two models with the same advection rates v_0, but a twofold difference in erodibility, highlights the effect of erosion on local relief, sediment flux, and the geomorphic expression of a legacy landscape. A twofold increase of K (more specifically K_f, equations (6a) and (6b); see also Text S1) at an advection rate of $v_0 = 20$ mm/year (model *M20b*) leads to the development of a legacy landscape with a fixed, asymmetric main drainage divide (Figure 7) in contrast to a model with the same advection rate but lower erodibility at 4.5 Ma (Figure 5). The total width of the legacy landscape is approximately the same as for model *M20a* (Figure 5) and is directly related to the magnitude of advection. As expected K_{sn} is lower compared to models with lower K (i.e., equation (2)). Advection-parallel interfluves are present, but their relief is subdued, masking the transition between the advected legacy landscape and the pre-existing lowland topography (compare regions at $x = 10$–30 km for the 20 mm/year models in Figure 7).

Similarly, a twofold reduction of K at an advection rate of $v_0 = 10$ mm/year (model *M10b*) results in the development of a legacy landscape with migrated main drainage divide (Figure 7) in contrast to a model with the same advection rate but higher erodibility at 4.5 Ma (Figure 4). The total width remains approximately equivalent to model *M10a* (Figure 4) at the same time step and advection rate. Lower values of K also lead to overall higher K_{sn} (i.e., equation (2)).

4.5. Variable Ramp Angles

Evaluating the influence of three different midcrustal ramp angles highlights the sensitivity of legacy landscapes to rock uplift magnitude and width. Ramp angles were changed for models running at an advection rate of $v_0 = 10$ mm/year (Figure 8; models *M10c* and *M10d*) without

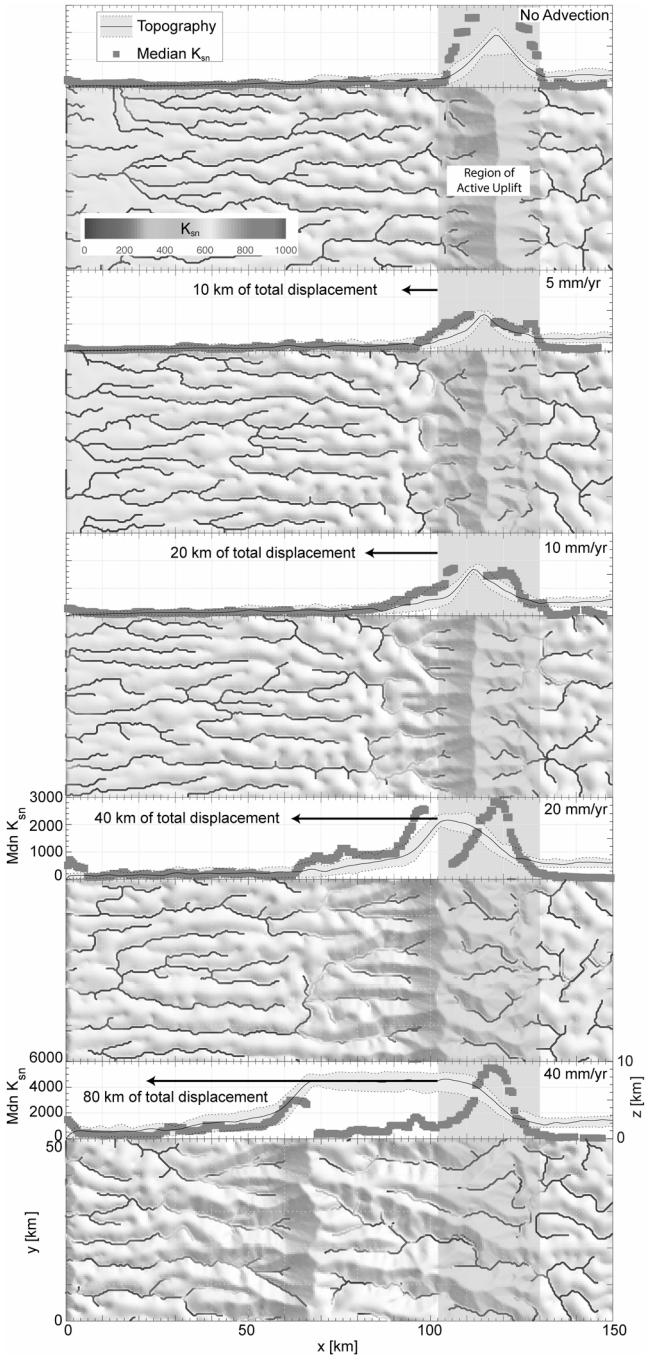

Figure 6. Simulated landscapes showing the evolution of topography and K_{sn} for varying advection rates ranging from $v_0 = 0$ mm/year ("No Advection") up to $v_0 = 40$ mm/year (models *M0, M5, M10a, M20a, and M40*, Tables 1 and 2) at a fixed model time of $t = 2$ Ma. The rock uplift rate for model *M0* "No Advection" corresponds to the same as for model *M20a* without the horizontal advection component. Models with $v_0 \leq 10$ mm/year are characterized by a main drainage divide within the region of active rock uplift, where legacy landscapes extend in the direction of advection, whereas models with $v_0 \geq 20$ mm/year contain migrated main drainage divides. Red vertical bar outlines region of active rock uplift. Mdn K_{sn}: median K_{sn}. Note change in vertical scale of K_{sn} for model at 40 mm/year.

changing the depth of the décollement (resulting in wider ramps for low angles). A fixed main drainage divide developed at $x \approx 112$ km and $x \approx 114$ km for ramp angles of $\alpha_r = 20°$ and $\alpha_r = 60°$, respectively, after 3 Myr; only slightly different to the location in the models shown in Figures 4–7 (middle row for reference; $\alpha_r = 40°$, model *M10a*). The range of modeled ramp angles encompasses those proposed or imaged for natural ramps (e.g., Allmendinger & Zapata, 2000; Bollinger et al., 2006; Boyer & Elliott, 1982; Kley, 1996; McQuarrie et al., 2008; Pandey et al., 1995; Rak et al., 2017; Tate et al., 2015; Whipple et al., 2016; Yue et al., 2005). At a lower ramp angle, more time is required to develop a stable divide, compared to the steeper ramp. The legacy landscape for all three ramp angles extends to ~25 km from the region of active rock uplift approximately corresponding to the total displacement prescribed at $t = 3$ Ma. Elevated K_{sn} across the legacy landscape are slightly higher with steeper ramp angles. The higher K_{sn} values are also accompanied by a higher gradient of K_{sn} in the direction over which these elevated values decrease.

In summary, changes in ramp angles between 20° and 60° only impart a minor change on the development of a legacy landscape. Steeper ramp angles appear to show a weak positive correlation with the magnitude of K_{sn} across the legacy landscape and the gradient at which K_{sn} declines in proximal streams.

5. Fluvial Response of Variably Sized Channels

Exploring the response of trunk and tributary streams to displacement over a midcrustal ramp may provide insights into understanding the development of a legacy landscape as observed in the simulated and natural landscapes and highlight different fluvial response times with respect to upstream drainage area (Figures 9 and 10). Separation into trunk and tributary streams used an upstream drainage area threshold of 60 km^2 in model DEMs, 50 km^2 for Nepal and Bolivia, and 60 km^2 for Taiwan.

In a model without lateral advection at model time 2 Ma (Figure 9a; $v_0 = 0$ mm/year, model M0) K_{sn} in trunk and tributary streams increases up to ~2,500 within the region of active rock uplift, whereas everywhere else K_{sn} has mostly adjusted to "background" values (<500). In the region of active rock uplift K_{sn} in proximal tributary streams is slightly higher than in trunk streams; in distal streams differences in K_{sn} are negligible except for streams closest to the main drainage divide ($x \approx 110$ km) where K_{sn} in tributary streams are higher relative to trunk streams. Outside the region of active rock uplift, K_{sn} in trunk streams, while overall low and near background (<500), is locally slightly higher relative to tributary streams (e.g., at $x \approx 70$–100 km and $x \approx 140$–150 km). Toward $x = 0$, K_{sn} in trunk streams increases at a higher gradient relative to tributary streams. In a model with lateral advection, at model time 0.25 Ma, and a total displacement of 2.5 km (Figure 9b; $v_0 = 10$ mm/year, $\alpha = 20°$, model *M10c*), trunk streams crossing the region of active rock uplift respond to lateral advection over the midcrustal ramp with an increase in K_{sn} of up to ~1,000 most prominently at $x \approx 100$–105 km, while K_{sn} in tributary streams has not significantly changed anywhere across the landscape as expected following equation (5). However, the second-order variation in K_{sn}, especially in distal trunk streams (15–100 km, Figure 9b), highlights that K_{sn} has not

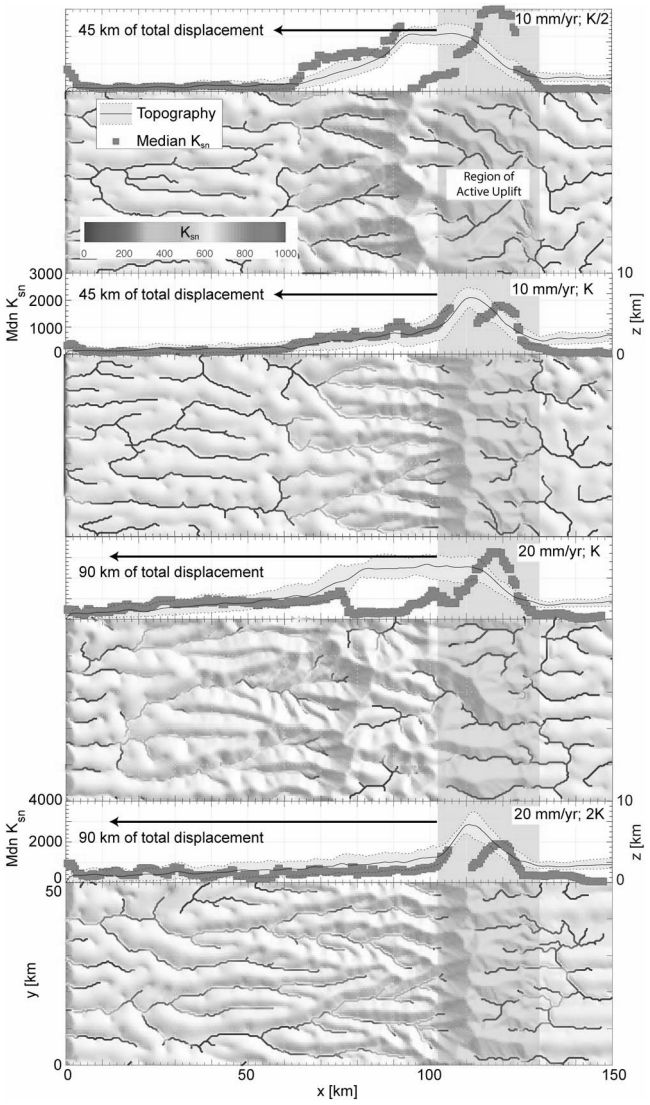

Figure 7. Comparison of simulated landscapes showing the evolution of topography and K_{sn} in map and cross-section views at 4.5 Ma varying erodibility by a factor of two. Models at v_0 = 10 mm/year (model *M10a*, Tables 1 and 2) and v_0 = 20 mm/year (model *M20b*) with twofold increased erodibility *K* develop legacy landscapes with fixed drainage divide. Models at v_0 = 20 mm/year (model *M20a*) and at v_0 = 10 mm/year (model *M10b*) with twofold decreased erodibility *K* develop legacy landscapes with migrated main drainage divide. Note the independence of legacy landscape widths from changes in *K*. Red vertical bar outlines region of active rock uplift. Mdn K_{sn}: median K_{sn}. Vertical scale of K_{sn} is the same for the same advection rates.

reached background (<500) values at this early stage in the model and that the topography here is still influenced by the initial topographic conditions (section 4.1). This indicates that the landscape is in the process of "decay" (i.e., influenced by the initial topographic conditions) in contrast to the "adjusted" model landscape (i.e., the influence by the initial topographic conditions is minor) in Figures 9a and 9c. A sharp increase in K_{sn} in the trunk streams at this time step is present in their downstream sections within the region of active rock uplift. A distinct drainage divide above the region of active rock uplift has not developed yet, and most trunk streams drain toward $x = 0$. At model time 3 Ma and a total displacement of 30 km (Figure 9c) a main drainage divide and a legacy landscape has emerged. K_{sn} in proximal trunk streams increases at a higher spatial gradient relative to proximal tributary streams and reach higher values of up to ~1,800 compared to ~900 in the tributary streams ($x \approx$ 125–140 km). K_{sn} drops to ~1,000 and ~600, respectively, when approaching the main drainage divide ($x \approx$ 114–125 km). Across the main drainage divide ($x \approx$ 100–108 km) distal tributary streams show higher K_{sn} (up to ~1,600) relative to distal trunk streams (up to ~1,400) and both decrease at approximately the same gradient to a value of ~300 (at $x \approx 100$), similar to the observed changes in K_{sn} across the main drainage divides in the models presented earlier. Within the legacy landscape a ~30-km wide section (e.g., $x \approx$ 70–100 km) exhibits slightly higher K_{sn} in trunk streams relative to tributary streams despite an assumingly faster response time in the former. A one-tailed Kolmogorov-Smirnov test comparing the distribution of K_{sn} between trunk and tributary streams supports the hypothesis that the distribution of K_{sn} in trunk streams have higher values than that in tributary streams (at a *5%* confidence level). The median difference in K_{sn} between trunk and tributary streams in the interval x = 10–50 km is lower (i.e., non-legacy landscape; $\Delta K_{sn} \approx 28$) than at x = 60–100 km (i.e., legacy landscape; $\Delta K_{sn} \approx 123$). At $x \approx$ 80–90 km both trunk and tributary streams decrease in K_{sn} but show a second-order variability which complicates assessing whether the change in gradient from K_{sn} values of ~300 to background is different between trunk and tributary streams. Beyond the region of active rock uplift and the legacy landscape, K_{sn} in all streams has mostly adjusted to background values (similar to Figure 9a, but in contrast to the early time step in Figure 9b). Increases in K_{sn} at $x \approx 0$ are interpreted as edge effects caused by the advection of potentially higher elevation topography into the zero-elevation boundary.

Suspected legacy landscapes in natural examples (Figure 10) show that trunk streams located between advection-parallel interfluves have higher K_{sn} relative to tributary streams, where this overall pattern is more pronounced than in the simulations. The K_{sn} distributions across the Bolivian Andes and the Nepalese Himalaya both show elevated K_{sn} in trunk and tributary streams that decline in the direction of advection. K_{sn} in trunk streams reach the highest values, are generally more irregular (peaks and troughs in K_{sn} over ~5- to 10-km distance) and decline at a steeper gradient than tributary streams (Figures 10a and 10b). In the case of Taiwan (Figure 10c), the difference between K_{sn} in trunk and tributary streams, and the overall magnitude in K_{sn}, is smaller. Similar to the larger orogens, elevated K_{sn} in trunk streams reach the highest values, and thus show a steeper decline in the direction of transport. K_{sn} in both trunk and tributary streams gradually decline over a distance of ~15–20 km and display marked peaks and troughs in K_{sn} over ~5-km distance. Notable differences in K_{sn} for both trunk and tributary streams are at ~12-, ~20-, and ~28-km distance along the section.

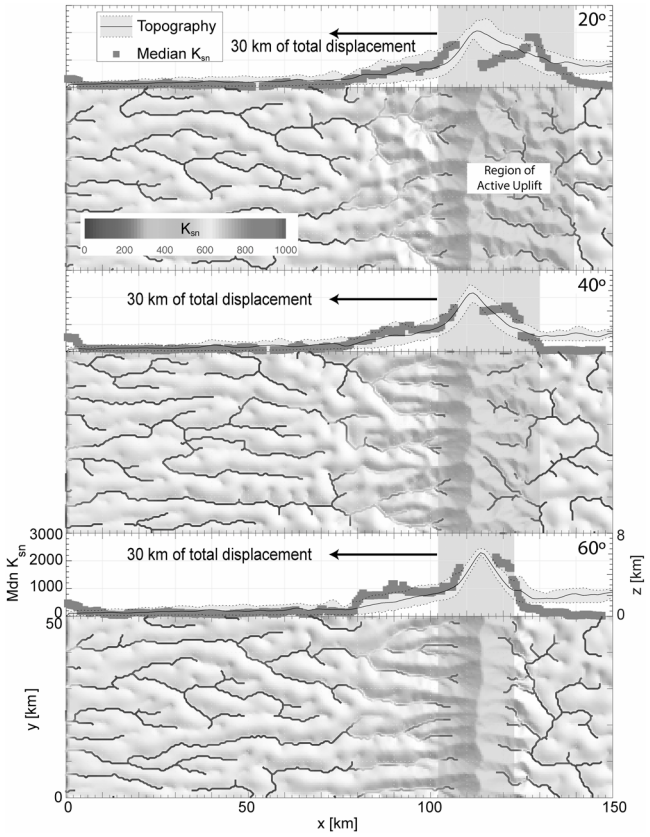

Figure 8. Simulated landscapes showing the evolution of topography and K_{sn} in map and cross-section views varying ramp angle for models with an advection rate of $v_0 = 10$ mm/year (top $\alpha_r = 20°$, model *M10c*; middle $\alpha_r = 40°$, model *M10a*; bottom $\alpha_r = 60°$ model *M10d*) at a model time step of $t = 3$ Ma. Note that only ramp widths, not ramp heights, have been changed. Red vertical bars outline region of active rock uplift. Mdn K_{sn}: median K_{sn}.

6. Discussion

6.1. Development of Legacy Landscapes in Convergent Orogens

The geomorphology of fold-thrust belts is mainly driven by the interaction between surface processes and the vertical and horizontal displacement of bedrock along active faults, which at an orogen scale is primarily expressed as a gradual decline in elevation (i.e., tapered topography) at the prowedge and retrowedge sides of an active convergent orogen such as in the Andes, Himalaya, or Taiwan (Figure 3c; e.g., Willett et al., 2001). Many models of orogen-scale convergence and landscape evolution typically assume a critically tapered wedge where shortening and rock uplift is occurring everywhere along the wedge (e.g., Willett et al., 2001). In contrast, mapped and seismically imaged active and inactive structures in fold-thrust belts highlight shortening by horizontal and vertical displacement along discrete fault planes where rock uplift is generated by motion over ramps along the décollement, out-of-sequence thrusting, and surface breaking faults. To produce high topography in the Himalaya or the Andes by rock uplift over discrete structures such as a ramp in the décollement requires that displacement over the ramp is maintained over millions of years. Thus, our model setup does not assume that rock uplift is generated through internal shortening above a critically tapered wedge. The models replicate displacement along an evolving fault system where steeper sections (i.e., ramps) are responsible for meaningful rock uplift, and flat décollements translate uplifted topography and elevated K_{sn} in the direction of transport (Figures 1 and 3). A double-vergent wedge geometry, as is the case in Timor and Taiwan, requires the evolution of opposite verging ramps (Figure 3c) that are proposed and imaged in these orogens (e.g., Tate et al., 2015; Yue et al., 2005).

Our numerical experiments suggest that lateral advection of uplifted topography creates a legacy landscape characterized by a tapered topography featuring high-relief, advection-parallel interfluves together with K_{sn} values that gradually decline to background levels away from the region of active rock uplift. This pattern is clearly recognizable after ~1–1.5 Myr of model time for convergence rates of $v_0 = 10$–20 mm/year with realistic values of K (e.g., Figures 4 and 5 and Movies S1 and S2). In addition to lateral advection, the magnitude of K_{sn} in a legacy landscape is further influenced by erodibility (Figure 7) and to a minor degree ramp angle (Figure 8). The simulation duration (1.5–5 Myr) is well within estimates of midcrustal ramp activity (~2–15 Myr) in the Andes (Garzione et al., 2017; Lease et al., 2016; McQuarrie et al., 2008; Rak et al., 2017) and the Himalaya (Hubbard et al., 2016; Long et al., 2012).

The width of a legacy landscape, as defined by the maximum extent of advection-parallel, high-relief interfluves, and elevated K_{sn} beyond the region of active rock uplift, is primarily controlled by the duration of advection over a ramp, and the rates of advection and erosion (Figure 11a; see also Figures 4 and 5). Equation (4a) further implies an inherent trade-off between advection rate and erodibility, as reflected by the nondimensional fluvial efficacy number ε (e.g., Miller et al., 2007; Willett et al., 2001). For a given advection rate, higher erodibility lowers the relief of the advected interfluves and decreases K_{sn} to background values limiting the recognition of the legacy landscape (Figure 7). Lower erosion rates will lead to legacy landscape widths closer to the total amount of displacement resulting in near linear relations between displacement of topography and time of ramp activity (Figures 11 and 12). Efficient erosion within a legacy landscape (e.g., due to more easily erodible bedrock and/or orographic precipitation) or low rates of advection relative to erosion (i.e., high fluvial efficacy numbers) may therefore mask the amount of displacement recorded by a legacy landscape. Thus, the width of legacy landscapes in convergent orogens may serve as a minimum estimate for the total displacement of topography since the initiation of a midcrustal ramp.

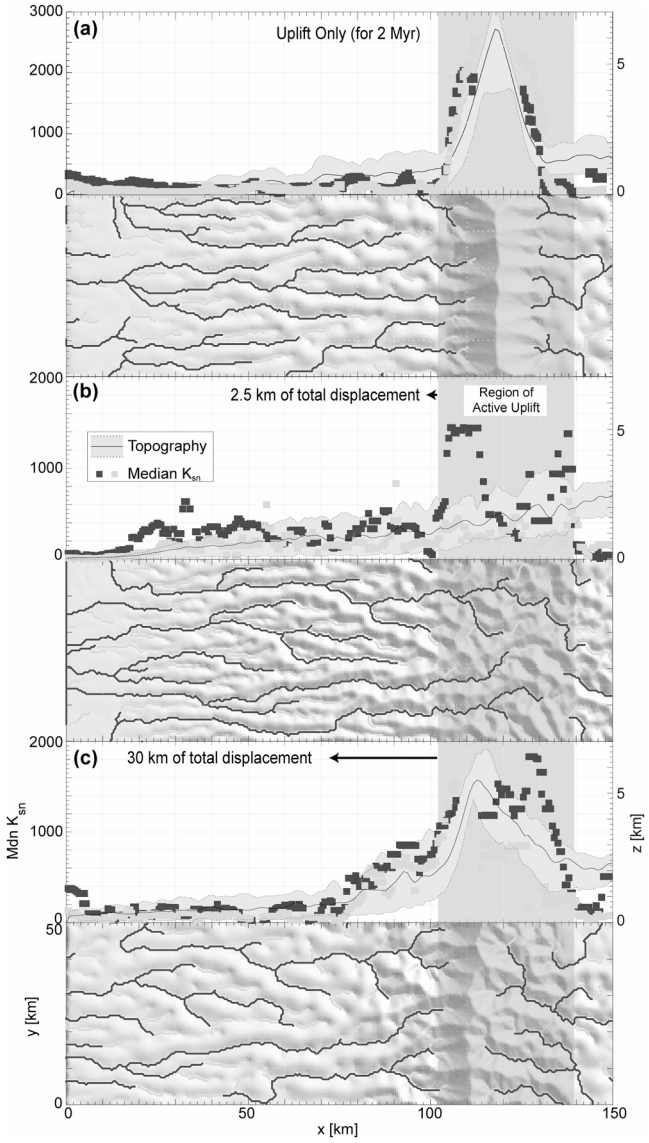

Figure 9. Differences in K_{sn} (profile views) in trunk (drainage area ≥60 km^2) and tributary (drainage area <60 km^2) streams (map view) for the "Uplift Only" model (a) at t = 2 Ma (model *M0*, Tables 1 and 2) and "advection" models at t = 0.25 Ma (b) and 3 Ma (c) (v_0 = 10 mm/year and α = 20°; model *M10c*, Tables 1 and 2). A one-tailed Kolmogorov-Smirnov test (5% confidence level) in the interval x = 50–100 km supports the hypothesis that the values in K_{sn} distributions of trunk streams are larger than those in tributary streams in all plots. Here and in all subsequent statistical tests, raw model K_{sn} values were smoothed over a five-point moving average filter prior to the statistical test. Median differences of K_{sn} (ΔK_{sn}) in trunk and tributary streams in this interval are $\Delta K_{sn} \approx 43$, $\Delta K_{sn} \approx 116$, and $\Delta K_{sn} \approx 104$, respectively. In (c) along the intervals x = 10–50 km (non-legacy landscape) and x = 60–100 km (i.e., legacy landscape) the differences in K_{sn} in trunk and tributary streams are $\Delta K_{sn} \approx 28$ and $\Delta K_{sn} \approx 123$, respectively. Red vertical bar outlines region of active rock uplift. Mdn K_{sn}: median K_{sn}.

Low fluvial efficacy numbers in our models (e.g., Figure 5 and equation (4a)) result in a migration of the main drainage divide beyond the region of active rock uplift in the direction of advection. Thus, a critical threshold ε_c may exist that distinguishes between a stable and a mobile main drainage divide in a region that experiences lateral advection (Figure S8). However, communication between the hillslope and fluvial domains may be a key component, not incorporated in ε (equation (4b)), that influences the mobility of the main drainage divide.

6.2. Implications of Landscape Response Time to Decay of Legacy Landscapes

The decay or rejuvenation of landscapes, and thus the long-term preservation of ancient mountain ranges such as the Appalachians, Alps, or Canadian Rockies, has been a matter of ongoing debate (e.g., Baldwin et al., 2003; Champagnac et al., 2009; Miller et al., 2013; Osborn et al., 2006). The preservation of legacy landscapes in our 2-D model experiments appears contradictory to the rapid response time of fluvial landscapes (e.g., equation (4a)); Whipple, 2001) as typically described by 1-D numerical and analytical models. This difference in response time between 2-D and 1-D models primarily reflects the lateral variability in flow direction over a 2-D landscape, where channels and interfluves are formed at sites of flow convergence and divergence, respectively. The resulting differences in discharge influence the ability of fluvial erosion to counterbalance the rock uplift caused by lateral advection of bedrock. In our experiments, these distal channels and interfluves stem from the main drainage divide (e.g., Figure 4 and Movies S1 and S2), where the interfluves are characterized by very low drainage area and hence by a slow fluvial response time (e.g., equation (5); see also Berlin & Anderson, 2007; Crosby & Whipple, 2006; Rosenbloom & Anderson, 1994; Shelef et al., 2018; Tucker & Whipple, 2002; Weissel & Seidl, 1998). When hillslope processes are slow, the advection of interfluves away from the ramp can form the elevated advection-parallel interfluves that are a key component of legacy landscapes (Figures 1 and 4). As the trunk streams between these interfluves incise, their drainage area and the local relief increases and so does the flux of sediments from the interfluves to the trunk streams. The increased sediment flux, in turn, can locally exceed the sediment transport capacity of these channels, causing localized deposition of alluvial material within the legacy landscape (Figure S10). Trunk streams respond to the increased sediment flux through an increase in their overall slope (e.g., Mackin, 1948; Simpson & Castelltort, 2012; Figure S10), for example, between locations of sediment deposition (and/or large rock-slope failures; Korup, 2006) and locations further downstream where no deposition occurs. The increase in drainage area in trunk streams due to horizontal advection relative to the stationary main drainage divide may also lead to an increased K_{sn}. As trunk streams increase their distance to the headwaters, drainage area also increases with continued horizontal advection (Figure 4 and Movie S1). If the rate of increase in drainage area in trunk streams is higher than the rate at which their slope adjusts to this increase, trunk K_{sn} would increase relative to adjacent tributary streams that are not advected relative to their own headwater. Such processes involving changes in drainage area and sediment flux due to lateral advection are likely to contribute to elevated and spatially fluctuating K_{sn} within trunk streams (e.g., Figures 9 and 10), as well as the observed spatial co-occurrence of high K_{sn} and elevated advection-parallel interfluves in legacy landscapes (e.g., Figure 9).

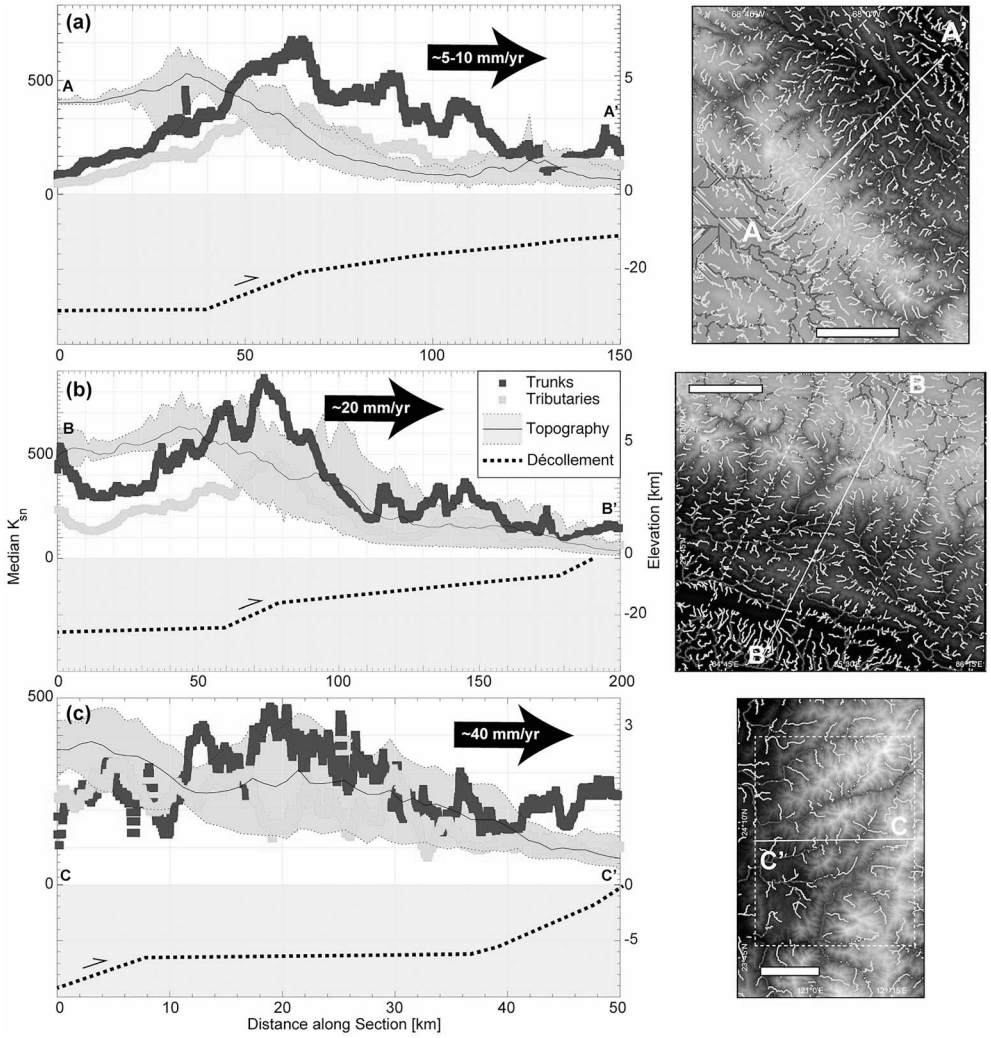

Figure 10. Distribution of K_{sn} (profile views in left column) in trunk and tributary streams (map views in right column) across the central Bolivian Andes (a), the central Nepalese Himalaya (b), and the Peikang River region in Taiwan (c) above proposed décollement geometries (McQuarrie et al., 2008; Whipple et al., 2016; Yue et al., 2005). A one-tailed Kolmogorov-Smirnov test (5% confidence level) along the sections supports the hypothesis that the values in K_{sn} distributions of trunk streams are larger than those in tributary streams in all plots. Scale bars on map views the same as in Figure 1. Drainage area thresholds are 50 km^2 for the Andes and Himalaya and 60 km^2 for Taiwan (slightly increased to better match the extent of trunk streams).

The presence of lateral advection exerts an important influence on the distribution of K_{sn} across simulated and natural landscapes. As pointed out by Miller et al. (2007), typical slope/area relationships may not apply when bedrock channels are advected through a region of active rock uplift. In our simulated landscapes, proximal streams that enter the region of active rock uplift initially show a commonly expected slope/area relationship, that is, the faster response of trunk streams in comparison to tributary streams (equation (5) and Figure 9b) leads to a more rapid increase in slope and thus K_{sn} (Figure 9c). However, the advection of these higher slopes in proximal streams closer to the main drainage divide lowers the effective rock uplift rate (i.e., the first two terms on the right-hand side of equation (3)) resulting in a drop in K_{sn} in both trunk and tributary streams as shown throughout our experiments (e.g., Figures 4 and 9b), with trunk streams maintaining a higher K_{sn} than tributary streams in our models. This phenomenon causes an opposite response in distal streams where the effective rock uplift rate is increased by the advection of steeper slopes away from the main drainage divide leading to an increase in K_{sn}, with tributary streams initially having higher K_{sn} than trunk streams near the divide in our models, after which K_{sn} gradually declines over the width of the legacy landscape.

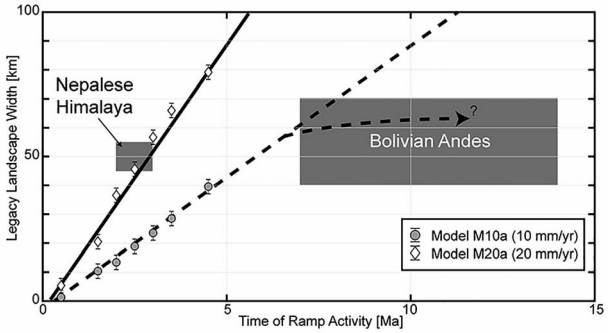

Figure 11. Relationship between the width of legacy landscapes measured from the region of active rock uplift and time shown for models *M10a* and *M20a*, where the slope corresponds to advection rate (see also Figures 4 and 5 and Tables 1 and 2). Locations for the central Nepalese Himalaya and central Bolivian Andes are based on estimates of their respective legacy landscape widths (Figure 12) and convergence rates (e.g., v_0 = 5–10 mm/year and v_0 = 20 mm/year, respectively).

In natural landscapes, such as the Andes, Bolivia, and Taiwan (Figures 1 and 10), K_{sn} in trunk streams has the highest values in the region of proposed active rock uplift (see Figures 1 and S5 for proposed locations of ramps; Elliott et al., 2016; Hubbard et al., 2016; McQuarrie et al., 2008; Whipple et al., 2016; Yue et al., 2005) and declines more rapidly in the direction of advection relative to tributary streams, in agreement with the relationship between drainage area and response time (equation (5); e.g., Figure 9b). Across the potential legacy landscapes K_{sn} is consistently higher in trunk streams than in tributary streams (Figure 10) while also behaving more erratically. The limited size of our model space and limited number of streams in each category (i.e., trunk and tributary streams) may preclude clearly seeing a similar relation in the simulated landscapes (Figure 9c).

The coexistence of advection-parallel interfluves and elevated K_{sn} in trunk and tributary streams across both modeled and natural landscapes strongly suggests these features are related. Across proposed natural legacy landscapes (Figure 12), the maximum extent of advection-parallel interfluves corresponds to regions of high local relief (Figures 1 and 12). Translated interfluves and the associated high relief provide a ready explanation for elevated K_{sn} in tributary streams (Figure 10). However, we suggest that the high relief interfluves also provide an increase in sediment flux in trunk streams (e.g., through increased landslide activity), potentially contributing to an increase in K_{sn} in trunk streams in both our simulated legacy landscapes (Figure S10), as well as natural landscapes. The ability of CASCADE to incorporate sediment flux and deposition (section 2.3 and Figure S10) means that it can capture the adjustment of trunk stream slopes to alluviated channel sections. The hypothesis, that increased sediment flux contributes to elevated K_{sn}, is supported by comparing models with high and low erodibility (e.g., Figure 7). When modeled streams are categorized into trunk and tributary streams, modeled landscapes with higher erodibility (e.g., 2 *K*) result in lower elevation interfluves, more closely spaced tributaries (e.g., Perron et al., 2009) with lower K_{sn}, but maintain elevated trunk K_{sn} values similar to those modeled with lower erodibility (*K*; Figure S9) consistent with an increase of sediment flux due to an increase in transport efficiency (i.e., higher erodibility leading to more erosion of the elevated interfluves and thus to increased sediment flux into the trunk streams). An increase in drainage area due to continued lateral advection may explain the consistently high K_{sn} values in trunk streams across natural legacy landscapes while the increase in sediment flux (potentially influenced by channel width;

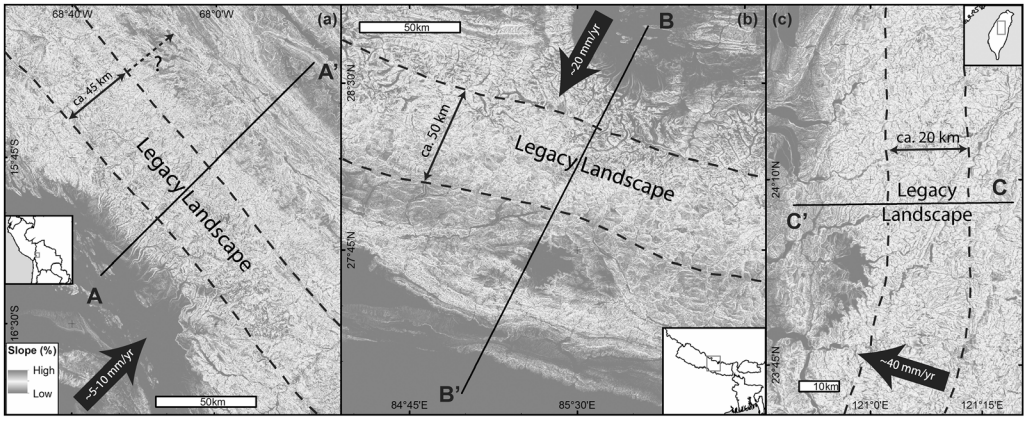

Figure 12. Local relief maps and identification of legacy landscapes capturing the extent of advection-parallel interfluves (see also relief maps in Movies S1–S3 for comparison) in the central Bolivian Andes (a), the central Nepalese Himalaya (b), and the Peikang River region in Taiwan (c; see also Figure 1). Based on the approximate widths of the legacy landscapes, midcrustal ramps have been active for at least ~7–14 Myr in the Andes (assuming v_0 = 5–10 mm/year), ~2.5 Myr for the Nepalese Himalaya (assuming v_0 = 20 mm/year), and ~0.5 Myr in Taiwan.

Amos & Burbank, 2007) may contribute to the K_{sn} values that are both high and more erratic. Pronounced changes in precipitation (e.g., Gasparini & Whipple, 2014) and varying lithology may also strongly influence sediment flux in these landscapes.

6.3. Present-Day Legacy Landscapes

Based on the results of our simulations, the presence of a legacy landscape in natural settings should occur under the following conditions: (i) a convergent tectonic regime and (ii) advection along a décollement over a midcrustal ramp over geologic time scales. These conditions are fulfilled most prominently across the present-day Bolivian Andes and the Nepalese Himalaya (Figures 1 and 10 and Table 3). Both fold-thrust belts show wide regions (>40 km) that are characterized by (i) an increased local relief featuring higher elevation advection-parallel interfluves and a tapered topography (Figures 1 and 12), (ii) a characteristic across-strike distribution of elevated K_{sn} that declines in the direction of convergence (Figures 1 and 10), (iii) visible differences in K_{sn} between trunk and tributary streams, and (vi) legacy landscape widths that are in accordance with proposed advection rates and locations of midcrustal ramps in the Andes (Garzione et al., 2017; Lease et al., 2016;McQuarrie et al., 2008; Rak et al., 2017) and the Himalaya (Elliott et al., 2016; Hubbard et al., 2016; Long et al., 2012; Whipple et al., 2016; see also Figure S5).

In the context of our model results, these metrics suggest that ~40–60 km of advected legacy landscape exists in these regions (Figures 1 and 12, Table 3; see also Figure S5 for proposed locations of midcrustal ramps; Elliott et al., 2016; McQuarrie et al., 2008; Whipple et al., 2016; Yue et al., 2005). The combination of high local relief featuring advection-parallel interfluves and elevated K_{sn} is particularly consistent in the Nepalese Himalaya (Wobus et al., 2003; Wobus, Whipple, & Hodges, 2006; Figures 1, 12, and S5; Whipple et al., 2016; Elliott et al., 2016). In the Bolivian Andes, K_{sn} declines at a lower spatial gradient than in the Himalayas, and the K_{sn} difference between trunk and tributary streams remains higher for a larger distance compared to the Nepalese Himalaya. This suggests that the fluvial system in the Bolivian Andes (low advection rate) responds slower than that in the Nepalese Himalaya (high advection rate) to changes in rock uplift as it exits the ramp. In the Peikang River region of Taiwan (Figure 10), the separation of K_{sn} in trunk and tributary streams is most pronounced between 10 and 40 km; however, both the magnitude of peak K_{sn} and the difference between K_{sn} values of trunk and tributary streams are notably smaller than exhibited in the Andes or the Nepalese Himalaya. The translated, elevated K_{sn} values argue for the presence of a legacy landscape albeit one that is either relatively young or rapidly decaying compared to Nepal and Bolivia (Figure 10).

Convergent orogens are subject to changes in bedrock erodibility, precipitation, convergence rate, and time since initial rock uplift. For example, convergence rates across the Andes are relatively low ($v_0 \approx$ 5–10 mm/year) compared to the Himalaya ($v_0 \approx$ 20 mm/year) and Taiwan ($v_0 \approx$ 40 mm/year). In addition, their dominant lithologies and magnitude of precipitation markedly differ (Table 3). The central Bolivian Andes are characterized by prolonged ramp activity at low convergence rates combined with high bedrock erodibility of regionally occurring sedimentary rocks, potentially enhanced by the steep precipitation gradient along the northeastern slopes of the Beni Escarpment in the direction of advection (further increasing erodibility and sediment flux within the legacy landscape). The width of the proposed legacy landscape is at least ~40 km, potentially up to 70 km (Figure 12a). The latter (~70 km) is similar to the amount of proposed horizontal displacement (~66–83 km) over a basement ramp (McQuarrie et al., 2008; Rak et al., 2017) and is most readily seen in the extent of elevated local relief (Figure 12). Lower widths (~40 to potentially 60 km) are determined from the distance between highest K_{sn} and the width of elevated K_{sn} above background (Figures 1 and S5). The difference between displacement amount and width of elevated K_{sn} may reflect an erosional decay of the advected topography. In contrast, extreme conditions such as low precipitation combined with low bedrock erodibility and long-term sustained convergence rates may have led to a migrating main drainage divide in the Andes in southern Bolivia (Figure S6). Other processes such as an increased rate of hillslope processes adjacent to an oversteepened main drainage divide, or frequent changes in the subsurface structural geometry may play a critical role in preventing the migration of main drainage divides in most other natural settings.

Previous studies attributed the distribution of gradually declining K_{sn} to a gradual decline in the rock uplift field in the direction of advection (Bolivia and Nepal, e.g., Gasparini & Whipple, 2014; Whipple et al., 2016;

Table 3
List of Legacy Landscapes in Natural Settings

Convergent orogen	Legacy landscape characteristics	Estimated activity of midcrustal ramp and general erodibility	Representative model(s)
Central Bolivian Andes	~40–60 km of legacy landscape with fixed drainage divide	7 to 14 Myr at 5–10 mm/year and increased erodibility (reflecting a combination of a strong orographic precipitation effect and higher bedrock erodibility for dominantly sedimentary rocks)	*M10a*, *M10c*, *M10d*, and *M5*
Nepalese Himalaya	~40–60 km of legacy landscape with fixed drainage divide	~2.5 Myr at ~20 mm/year and enhanced erodibility due to strong orographic precipitation effects (potentially combined with weaker Lesser Himalayan bedrock material)	*M20b* and *M20c*
Taiwan (Peikang River Region)	~15–20 km of legacy landscape with fixed drainage divide	~15 Myr at >40 mm/year (Sibuet et al., 2002) and very high erodibility caused by intense wet climate	*M40* at high erodibility (not modelled)
Southern Bolivian Andes	~40–60 km legacy landscape with migrated drainage divide	7 to 14 Myr at 5–10 mm/year and overall low erodibility (potentially reflecting a combination of weak orographic precipitation effects and lower bedrock erodibility)	*M10b*

Wobus, Whipple, & Hodges, 2006) or a complex suite of structural geometries (eastern Greater Caucasus, e.g., Forte et al., 2015). However, our simulations qualitatively reproduce the suite of first-order geomorphic observation from natural settings (i.e., high relief, advection-parallel interfluves, tapered topography, and a gradual decline of K_{sn} in the direction of advection). To a certain degree, the models also reproduce second-order geomorphic features such as different patterns of K_{sn} versus distance for trunk and tributary streams. Based on our model results this variation in K_{sn} between trunk and tributary streams suggests differential fluvial response times (using drainage area as proxy for fluvial response time) and implies that high K_{sn} in trunk streams relative to tributary streams are a result of increased sediment flux and changing drainage area due to continued lateral advection and does not require laterally changing precipitation, for example, due to orographic effects (Gasparini & Whipple, 2014). These geomorphic features are the topographic response to a simple and common structural geometry: advection over a steeper ramp followed by translation along a flat décollement. Thus, a decline in rock uplift or complex fault geometries are not necessary to explain the gradual decline of elevated K_{sn} in the direction of advection. In addition, the emergence of an orogen-scale tapered topography due to advection over a midcrustal ramp removes the need for continued and systematic rock uplift everywhere along the orogenic wedge to create the characteristic tapered topography of compressional orogens.

6.4. Limitations and Future Directions

Even though our study demonstrates the emergence of legacy landscapes, it cannot address the full complexity of natural landscapes and/or explore systematically all the relevant variables that may influence the geomorphic response in convergent orogens. Below, we point at some of the limitations of our approach and suggest future directions that can advance the overall understanding of landscape development in convergent orogens. First, we assume an idealized structural framework by analyzing the geomorphic response to advection along a décollement over a single midcrustal ramp. Fold-thrust belts, however, commonly develop over geologic time above an evolving décollement, which includes in-sequence activation of ramps, multiple ramps, out-of-sequence thrusting, and/or normal faulting and surface breaking faults. These more complicated structural features are not accounted for here and would be superimposed on the fundamental geomorphic response we show (e.g., Figure S7). We also assumed no along-strike changes in fault geometry

or convergence rates. Careful mapping of faults and documentation of exhumation patterns through time, for example, aided by thermochronology, can illuminate more complex geometries in regions where a legacy landscape is suspected. Second, our simulations assume idealized channel geometry (i.e., Yanites & Tucker, 2010), spatially and temporally constant precipitation and lithology, and a prescribed initial fluvial network prior to each simulation. However, given that in natural settings these parameters can change in space and/or time, simulations that incorporate such changes may assess their influence on the formation of legacy landscapes and the geomorphic features (e.g., translated interfluves and gradually decreasing K_{sn}) used to identify them. Lithology, for example, particularly where vertical displacement components are small, may profoundly affect the geomorphology in an advection setting (e.g., Forte et al., 2016; Perne et al., 2017). Third, the choice of the surface processes model (in our case the model by Kooi & Beaumont, 1994) may yield different results. A systematic comparison between strictly detachment-limited and combined detachment- and transport-limited models in a similar structural framework may provide more detailed insights into the relative contributions of increased sediment flux and changing drainage area due to lateral advection on high K_{sn} in legacy landscapes, particularly in trunk streams. Further insight can be gained through field-based exploration of the relations between increased sediment flux from elevated interfluves, transport-limited reaches in trunk streams, and high K_{sn} values. Fourth, the interaction of the hillslope and fluvial domains likely plays an important role in the preservation of advection-parallel interfluves and the mobility of the main drainage divide. Although we have not explicitly tested it, a relatively slow hillslope response time may be an additional key requirement for the emergence of legacy landscapes. A systematic exploration of different types and magnitudes of hillslope processes will help constraining the influence of these interactions on legacy landscapes. Furthermore, our simulations suggest a potential fluvial efficacy threshold (Figure S8) that presumably distinguishes between mobile and fixed main drainage divides, but natural examples appear rare (Figure S7), and our hypotheses regarding the role of hillslope processes in such settings remain untested.

7. Concluding Remarks

Lateral advection over a décollement is crucial to explain the geologic evidence of hundreds of kilometers of crustal shortening across major convergent orogens such as the Andes, Himalaya, or Taiwan. Discrete sections of the décollement are characterized by a steeper inclination (i.e., ramps), which cause high rock uplift rates and elevation.

Our integration of simple structural kinematics with 2-D numerical landscape evolution models reveals that advection along a décollement over a midcrustal ramp leads to the development of a transient legacy landscape beyond the region of active rock uplift in the direction of advection. This legacy landscape is characterized by an orogen-scale gradual decline in topography, which is expressed as high-relief advection-parallel interfluves extending beyond the region of active rock uplift, elevated and gradually declining K_{sn} values, and characteristic differences in magnitudes of K_{sn} in channels of large and small drainage area. The width of this legacy landscape provides a minimum estimate for the amount of lateral advection since initiation of ramp activity and is primarily controlled by the duration of ramp activity and the rates of advection and erosion.

The development of legacy landscapes is interpreted to reflect the coexistence, interaction, and response of individual landscape components, including differently sized fluvial channels and interfluves formed through the lateral variability in flow convergence, features that are not captured in idealized 1-D models. Higher K_{sn} in large streams relative to small ones highlights the transient nature of legacy landscapes and may reflect the increased sediment flux from high-relief, advection-parallel interfluves, and increase in drainage area due to lateral advection.

We show that the gradual decline of elevated K_{sn} values toward the foreland and their association with broad (~15–60 km) regions of increased local relief and orogen-scale tapered topography in active fold-thrust belts, such as the Nepalese Himalaya, Bolivian Andes, or Taiwan, can be explained by the tectonic advection of topography over midcrustal ramps along a décollement. Our findings provide an alternative to previously suggested mechanisms that would require regions of gradually declining rock uplift over large distances or complex subsurface fault geometries.

Acknowledgments

Paul R. Eizenhöfer is grateful for support through a Feodor-Lynen Postdoctoral Scholarship awarded to him by the Alexander von Humboldt Foundation and financial support by the University of Pittsburgh. We appreciate comments and insights from Kelin Whipple on early drafts of the manuscript. Scott Miller, Adam Forte, and an anonymous reviewer provided perceptive comments and suggestions that meaningfully improved the manuscript. The Editors John M. Buffington and Amy East and Associate Editor David Egholm are thanked for additional comments and the professional handling of the manuscript. We thank Willi Kappler (University of Tübingen) for support in conducting the simulations presented in this study. Todd A. Ehlers acknowledges support from a European Research Council consolidator grant (615703) that partially supported this work. We thank Midland Valley (https://www.mve.com) and Petroleum Experts (http://www.petex.com) for providing us access to their structural modeling software MOVE™. Model DEMs can be reproduced by the freely available landscape evolution algorithm CASCADE following the model set up and parameters described here. The original version of CASCADE is available from Jean Braun (https://github.com/jeanbraun/Cascade.git), whereas the modified version used in this study can be accessed as a branch (https://github.com/willi-kappler/Cascade). Model and natural DEM data analysis can be reproduced using the publicly available MATLAB® code TopoToolbox V2 (https://topotoolbox.wordpress.com).

References

Adams, B. A., Whipple, K. X., Hodges, K. V., & Heimsath, A. M. (2016). In situ development of high-elevation, low-relief landscapes via duplex deformation in the Eastern Himalayan hinterland, Bhutan. *Journal of Geophysical Research: Earth Surface*, *121*, 294–319. https://doi.org/10.1002/2015JF003508

Allmendinger, R. W., & Zapata, T. R. (2000). The footwall ramp of the Subandean decollement, northernmost Argentina, from extended correlation of seismic reflection data. *Tectonophysics*, *321*(1), 37–55. https://doi.org/10.1016/S0040-1951(00)00077-9

Amos, C. B., & Burbank, D. W. (2007). Channel width response to differential uplift. *Journal of Geophysical Research*, *112*, F02010. https://doi.org/10.1029/2006JF000672

Baldwin, J. A., Whipple, K. X., & Tucker, G. E. (2003). Implications of the shear stress river incision model for the timescale of postorogenic decay of topography. *Journal of Geophysical Research*, *108*(B3), 2158. https://doi.org/10.1029/2001JB000550

Berlin, M. M., & Anderson, R. S. (2007). Modeling of knickpoint retreat on the Roan Plateau, western Colorado. *Journal of Geophysical Research*, *112*, F03SO6. https://doi.org/10.1029/2006JF000553

Bollinger, L., Henry, P., & Avouac, J. P. (2006). Mountain building in the Nepal Himalaya: Thermal and kinematic model. *Earth and Planetary Science Letters*, *244*(1-2), 58–71. https://doi.org/10.1016/j.epsl.2006.01.045

Boyer, S. E., & Elliott, D. (1982). Thrust systems. *AAPG Bulletin*, *66*(9), 1196–1230.

Braun, J., & Sambridge, M. (1997). Modelling landscape evolution on geological time scales: A new method based on irregular spatial discretization. *Basin Research*, *9*(1), 27–52. https://doi.org/10.1046/j.1365-2117.1997.00030.x

Braun, J., Zwartz, D., & Tomkin, J. H. (1999). A new surface-processes model combining glacial and fluvial erosion. *Annals of Glaciology*, *28*, 282–290. https://doi.org/doi:10.3189/172756499781821797

Burchfiel, B. C., Zhiliang, C., Yupinc, L., & Royden, L. H. (1995). Tectonics of the Longmen Shan and adjacent regions, Central China. *International Geology Review*, *37*(8), 661–735. https://doi.org/10.1080/00206819509465424

Champagnac, J.-D., Schlunegger, F., Norton, K., von Blanckenburg, F., Abbühl, L. M., & Schwab, M. (2009). Erosion-driven uplift of the modern Central Alps. *Tectonophysics*, *474*(1-2), 236–249. https://doi.org/10.1016/j.tecto.2009.02.024

Crosby, B. T., & Whipple, K. X. (2006). Knickpoint initiation and distribution within fluvial networks: 236 waterfalls in the Waipaoa River, North Island, New Zealand. *Geomorphology*, *82*(1–2), 16–38. https://doi.org/10.1016/j.geomorph.2005.08.023

Culling, W. E. H. (1960). Analytical Theory of Erosion. *The Journal of Geology*, *68*(3), 336344. https://doi.org/10.1086/626663

Duvall, A., Kirby, E., Burbank, D. (2004). Tectonic and lithologic controls on bedrock channel profiles and processes in coastal California. *Journal of Geophysical Research*, *109*, F03002. https://doi.org/10.1029/2003JF000086

Egan, S. S., Buddin, T. S., Kane, S. J., & Williams, G. D. (1997). Three-dimensional modelling and visualisation in structural geology: New techniques for the restoration and balancing of volumes. In *Proceedings of the 1996 Geoscience Information Group Conference on Geological Visualisation. Electronic Geology Special Volume* (Vol. 1, pp. 67-82).

Elliott, J. R., Jolivet, R., González, P. J., Avouac, J. P., Hollingsworth, J., Searle, M. P., & Stevens, V. L. (2016). Himalayan megathrust geometry and relation to topography revealed by the Gorkha earthquake. *Nature Geoscience*, *9*(2), 174–180. https://doi.org/10.1038/ngeo2623

Fernandes, N. F., & Dietrich, W. E. (1997). Hillslope evolution by diffusive processes: The timescale for equilibrium adjustments. *Water Resources Research*, *33*(6), 1307–1318. https://doi.org/10.1029/97WR00534

Flint, J. J. (1974). Stream gradient as a function of order, magnitude, and discharge. *Water Resources Research*, *10*(5), 969–973. https://doi.org/10.1029/WR010i005p00969

Forte, A. M., Cowgill, E., & Whipple, K. X. (2014). Transition from a singly vergent to doubly vergent wedge in a young orogen: The Greater Caucasus. *Tectonics*, *33*, 2077–2101. https://doi.org/10.1002/2014TC003651

Forte, A. M., Whipple, K. X., & Cowgill, E. (2015). Drainage network reveals patterns and history of active deformation in the eastern Greater Caucasus. *Geosphere*, *11*(5), 1343–1364. https://doi.org/10.1130/GES01121.1

Forte, A. M., Yanites, B. J., & Whipple, K. X. (2016). Complexities of landscape evolution during incision through layered stratigraphy with contrasts in rock strength. *Earth Surface Processes and Landforms*, *41*(12), 1736–1757. https://doi.org/10.1002/esp.3947

Garzione, C. N., McQuarrie, N., Perez, N. D., Ehlers, T. A., Beck, S. L., Kar, N., et al. (2017). Tectonic evolution of the Central Andean plateau and implications for the growth of plateaus. *Annual Review of Earth and Planetary Sciences*, *45*(1), 529–559. https://doi.org/10.1146/annurev-earth-063016-020612

Gasparini, N. M., & Whipple, K. X. (2014). Diagnosing climatic and tectonic controls on topography: Eastern flank of the northern Bolivian Andes. *Lithosphere*, 230–250. https://doi.org/10.1130/L322.1

Hack, J. T. (1957). Studies of longitudinal stream profiles in Virginia and Maryland. *USGS Professional Paper 249*, 97.

Mackin, J. (1948). Concept of the graded river. *Geological Society of America Bulletin*, *59*(5), 463–512. https://doi.org/10.1130/0016-7606(1948)59[463:COTGR]2.0.CO;2

Howard, A. D. (1994). A detachment limited model of drainage basin evolution. *Water Resources Research*, *30*(7), 2261–2285. https://doi.org/10.1029/94WR00757

Howard, A. D., & Kerby, G. (1983). Channel changes in badlands. *Geological Society of America Bulletin*, *94*(6), 739–752. https://doi.org/10.1130/0016-7606(1983)94<739:CCIB>2.0.CO;2

Hubbard, J., Almeida, R., Foster, A., Sapkota, S. N., Bürgi, P., & Tapponnier, P. (2016). Structural segmentation controlled the 2015 Mw 7.8 Gorkha earthquake rupture in Nepal. *Geology*, *44*(8), 639–642. https://doi.org/10.1130/G38077.1

Hurst, M. D., Mudd, S. M., Walcott, R., Attal, M., & Yoo, K. (2012). Using hilltop curvature to derive the spatial distribution of erosion rates. *Journal of Geophysical Research*, *117*, F02017. https://doi.org/10.1029/2011JF002057

Kane, S. J., Williams, G. D., Buddin, T. S., Egan, S. S., & Hodgetts, D. (1997). Flexural-slip based restoration in 3D, a new approach. In *1997 AAPG Annual Convention Official Program A* (Vol. 58).

Kirby, E., & Ouimet, W. (2011). Tectonic geomorphology along the eastern margin of Tibet: insights into the pattern and processes of active deformation adjacent to the Sichuan Basin. *Geological Society, London, Special Publications*, *353*(1), 165–188. https://doi.org/10.1144/SP353.9

Kirby, E., Regalla, C., Ouimet, W. B., & Bierman, P. R. (2010). Reconstructing temporal variations in fault slip from footwall topography: An example from Saline Valley, California. In *AGU Fall Meeting Abstracts*.

Kirby, E., & Whipple, K. (2001). Quantifying differential rock-uplift rates via stream profile analysis. *Geology*, *29*(5), 415–418. https://doi.org/10.1130/0091-7613(2001)029<0415:QDRURV>2.0.CO;2

Kirby, E., & Whipple, K. X. (2012). Expression of active tectonics in erosional landscapes. *Journal of Structural Geology*, *44*, 54–75. https://doi.org/10.1016/j.jsg.2012.07.009

Kirby, E., Whipple, K. X., Tang, W., & Chen, Z. (2003). Distribution of active rock uplift along the eastern margin of the Tibetan Plateau: Inferences from bedrock channel longitudinal profiles. *Journal of Geophysical Research*, *108*(B4), 2217. https://doi.org/10.1029/2001JB000861

Kley, J. (1996). Transition from basement-involved to thin-skinned thrusting in the Cordillera Oriental of southern Bolivia. *Tectonics*, *15*(4), 763–775. https://doi.org/10.1029/95TC03868

Kooi, H., & Beaumont, C. (1994). Escarpement evolution on hight-elevation rifted margins: Insights derived from a surface processes model that combines diffusion, advection, and reaction. *Journal of Geophysical Research*, *99*(B6), 12191–12209. https://doi.org/10.1029/94JB00047

Korup, O. (2006). Rock-slope failure and the river long profile. *Geology*, *34*(1), 45–48. https://doi.org/10.1130/G21959.1

Lague, D., Crave, A., & Davy, P. (2003). Laboratory experiments simulating the geomorphic response to tectonic uplift. *Journal of Geophysical Research*, *108*(B1), 2008. https://doi.org/10.1029/2002JB001785

Lease, R. O., Ehlers, T. A., & Enkelmann, E. (2016). Large along-strike variations in the onset of Subandean exhumation: Implications for Central Andean orogenic growth. *Earth and Planetary Science Letters*, *451*, 62–76. https://doi.org/10.1016/j.epsl.2016.07.004

Long, S. P., McQuarrie, N., Tobgay, T., Coutand, I., Cooper, F. J., Reiners, P. W., et al. (2012). Variable shortening rates in the eastern Himalayan thrust belt, Bhutan: Insights from multiple thermochronologic and geochronologic data sets tied to kinematic reconstructions. *Tectonics*, *31*, TC5004. https://doi.org/10.1029/2012TC003155

McClay, K. R. (1992). Glossary of thrust tectonic terms. In K. R. McClay (Ed.), *Thrust tectonics*, (pp. 419–434). London: Chapman & Hall. https://doi.org/10.1007/978-94-011-3066-0

McQuarrie, N., Barnes, J. B., & Ehlers, T. A. (2008). Geometric, kinematic, and erosional history of the central Andean Plateau, Bolivia (15–17° S). *Tectonics*, *27*, TC3007. https://doi.org/10.1029/2006TC002054

McQuarrie, N., & Ehlers, T. A. (2015). Influence of thrust belt geometry and shortening rate on thermochronometer cooling ages: Insights from thermokinematic and erosion modeling of the Bhutan Himalaya. *Tectonics*, *34*, 1055–1079. https://doi.org/10.1002/2014TC003783

McQuarrie, N., & Ehlers, T. A. (2017). Techniques for understanding fold-and-thrust belt kinematics and thermal evolution. In *Linkages and Feedbacks in Orogenic Systems: Geological Society of America Memoir* (Vol. 213, p. 25–54). https://doi.org/10.1130/2017.1213(02)

Miller, S. R., Sak, P. B., Kirby, E., & Bierman, P. R. (2013). Neogene rejuvenation of central Appalachian topography: Evidence for differential rock uplift from stream profiles and erosion rates. *Earth and Planetary Science Letters*, *369*, 1–12.

Miller, S. R., Slingerland, R. L., & Kirby, E. (2007). Characteristics of steady state fluvial topography above fault-bend folds. *Journal of Geophysical Research*, *112*, F04004. https://doi.org/10.1029/2007JF000772

Moon, S., Shelef, E., & Hilley, G. E. (2015). Recent topographic evolution and erosion of the deglaciated Washington Cascades inferred from a stochastic landscape evolution model. *Journal of Geophysical Research: Earth Surface*, *120*, 856–876. https://doi.org/10.1002/2014JF003387

Osborn, G., Stockmal, G., & Haspel, R. (2006). Emergence of the Canadian Rockies and adjacent plains: A comparison of physiography between end-of-Laramide time and the present day. *Geomorphology*, *75*(3-4), 450–477. https://doi.org/10.1016/j.geomorph.2005.07.032

Pandey, M. R., Tandukar, R. P., Avouac, J. P., Lave, J., & Massot, J. P. (1995). Interseismic strain accumulation on the Himalayan crustal ramp (Nepal). *Geophysical Research Letters*, *22*(7), 751–754. https://doi.org/10.1029/94GL02971

Perne, M., Covington, M. D., Thaler, E. A., & Myre, J. M. (2017). Steady state, erosional continuity, and the topography of landscapes developed in layered rocks. *Earth Surface Dynamics*, *5*(1), 85–100. https://doi.org/10.5194/esurf-5-85-2017

Perron, J. T., Kirchner, J. W., & Dietrich, W. E. (2009). Formation of evenly spaced ridges and valleys. *Nature*, *460*(7254), 502–505. https://doi.org/10.1038/nature08174

Perron, J. T., & Royden, L. (2013). An integral approach to bedrock river profile analysis. *Earth Surface Processes and Landforms*, *38*(6), 570–576. https://doi.org/10.1002/esp.3302

Rak, A. J., McQuarrie, N., & Ehlers, T. A. (2017). Kinematics, exhumation, and sedimentation of the north central Andes (Bolivia): An integrated thermochronometer and thermokinematic modeling approach. *Tectonics*, *36*, 2524–2554. https://doi.org/10.1002/2016TC004440

Rosenbloom, N. A., & Anderson, R. S. (1994). Hillslope and channel evolution in a marine terraced landscape, Santa Cruz, California. *Journal of Geophysical Research*, *99*(B7), 14013–14029. https://doi.org/10.1029/94JB00048

Royden, L., & Perron, J. T. (2013). Solutions of the stream power equation and application to the evolution of river longitudinal profiles. *Journal of Geophysical Research: Earth Surface*, *118*, 497–518. https://doi.org/10.1002/jgrf.20031

Royden, L. H. (1997). Surface deformation and lower crustal flow in Eastern Tibet. *Science*, *276*(5313), 788–790. https://doi.org/10.1126/science.276.5313.788

Schwanghart, W., & Kuhn, N. J. (2010). TopoToolbox: A set of Matlab functions for topographic analysis. *Environmental Modelling & Software*, *25*(6), 770–781. https://doi.org/10.1016/j.envsoft.2009.12.002

Schwanghart, W., & Scherler, D. (2014). TopoToolbox 2–MATLAB-based software for topographic analysis and modeling in Earth surface sciences. *Earth Surface Dynamics*, *2*(1), 1–7. https://doi.org/10.5194/esurf-2-1-2014

Shelef, E., Haviv, I., & Goren, L. (2018). A potential link between waterfall recession rate and bedrock channel concavity. *Journal of Geophysical Research: Earth Surface*, *123*, 905–923. https://doi.org/10.1002/2016JF004138

Shen, Z. K., Sun, J., Zhang, P., Wan, Y., Wang, M., Bürgmann, R., et al. (2009). Slip maxima at fault junctions and rupturing of barriers during the 2008 Wenchuan earthquake. *Nature Geoscience*, *2*(10), 718–724. https://doi.org/10.1038/ngeo636

Simpson, G., & Castelltort, S. (2012). Model shows that rivers transmit high-frequency climate cycles to the sedimentary record. *Geology*, *40*(12), 1131–1134. https://doi.org/10.1130/G33451.1

Sibuet, J.-C., Hsu, S.-K., Le Pichon, X., Le Formal, J.-P., Reed, D., Moore, G., & Liu, C.-S. (2002). East Asia plate tectonics since 15 Ma: constraints from the Taiwan region. *Tectonophysics*, *344*(1–2), 103134. https://doi.org.10.1016/s0040-1951(01)00202-5

Snyder, N. P., Whipple, K. X., Tucker, G. E., & Merritts, D. J. (2000). Landscape response to tectonic forcing: Digital elevation model analysis of stream profiles in the Mendocino triple junction region, northern California. *Geological Society of America Bulletin*, *112*(8), 1250–1263. https://doi.org/10.1130/0016-7606(2000)112<1250:LRTTFD>2.0.CO;2

Snyder, N. P., Whipple, K. X., Tucker, G. E., & Merritts, D. J. (2003a). Channel response to tectonic forcing: Field analysis of stream morphology and hydrology in the Mendocino triple junction region, northern California. *Geomorphology*, *53*(1–2), 97–127. https://doi.org/10.1016/S0169-555X(02)00349-5

Snyder, N. P., Whipple, K. X., Tucker, G. E., & Merritts, D. J. (2003b). Importance of a stochastic distribution of floods and erosion thresholds in the bedrock river incision problem. *Journal of Geophysical Research*, *108*(B2), 2117. https://doi.org/10.1029/2001JB001655

Stockmal, G. S., Beaumont, C., Nguyen, M., & Lee, B. (2007). Mechanics of thin-skinned fold-and-thrust belts: Insights from numerical models. In *special paper 433: Whence the mountains? Inquiries into the evolution of orogenic systems: A volume in honor of Raymond A. Price*, (Vol. 433, pp. 63–98). America: Geological Society. https://doi.org/10.1130/2007.2433(04)

Tate, G. W., McQuarrie, N., van Hinsbergen, D. J., Bakker, R. R., Harris, R., & Jiang, H. (2015). Australia going down under: Quantifying continental subduction during arc-continent accretion in Timor-Leste. *Geosphere*, *11*(6), 1860–1883. https://doi.org/10.1130/GES01144.1

Tucker, G. E., & Whipple, K. X. (2002). Topographic outcomes predicted by stream erosion models: Sensitivity analysis and intermodel comparison. *Journal of Geophysical Research*, *107*(B9), 2179. https://doi.org/10.1029/2001JB000162

U.S./Japan ASTER Science Team. 10.5067/ASTER/ASTGTM.002. see also, Abrams, M (2000). The Advanced Spaceborne Thermal Emission and Reflection Radiometer (ASTER): Data products for the high spatial resolution imager on NASA's Terra platform. *International Journal of Remote Sensing*, *21*(5), 847–859. https://doi.org/10.1080/014311600210326

Weissel, J. K., & Seidl, M. A. (1998). Inland propagation of erosional escarpments and river profile evolution across the southeast Australian passive continental margin. In J. Tinkler, & E. Wohl (Eds.), *Rivers Over Rock: Fluvial Processes in Bedrock Channels*, *Geophys. Monogr. Ser.*, (Vol. 107, pp. 189–206). Washington, D. C: American Geophysical Union. https://doi.org/10.1029/GM107p0189

Whipple, K. X. (2001). Fluvial landscape response time: How plausible is steady-state denudation? *American Journal of Science*, *301*(4–5), 313–325. https://doi.org/10.2475/ajs.301.4-5.313

Whipple, K. X., Hancock, G. S., & Anderson, R. S. (2000). River incision into bedrock: Mechanics and relative efficacy of plucking, abrasion, and cavitation. *Bulletin of the Geological Society of America*, *112*(3), 490–503. https://doi.org/10.1130/0016-7606(2000)112<490:RIIBMA>2.0.CO;2

Whipple, K. X., Shirzaei, M., Hodges, K. V., & Ramon Arrowsmith, J. (2016). Active shortening within the Himalayan orogenic wedge implied by the 2015 Gorkha earthquake. *Nature Geoscience*, *9*(9), 711–716. https://doi.org/10.1038/ngeo2797

Whipple, K. X., & Tucker, G. E. (1999). Dynamics of the stream-power river incision model: Implications for height limits of mountain ranges, landscape response timescales, and research needs. *Journal of Geophysical Research*, *104*(B8), 17661–17674. https://doi.org/10.1029/1999JB900120

Willett, S. D., & Brandon, M. T. (2002). On steady state in mountain belts. *Geology*, *30*(2), 175–178. https://doi.org/10.1130/0091-7613(2002)030<0175

Willett, S. D., McCoy, S. W., Perron, J. T., Goren, L., & Chen, C. Y. (2014). Dynamic reorganization of river basins. *Science*, *343*(6175), 1248765. https://doi.org/10.1126/science.1248765

Willett, S. D., Slingerland, R., & Hovius, N. (2001). Uplift, shortening, and steady state topography in active mountain belts. *American Journal of Science*, *301*(4–5), 455–485. https://doi.org/10.2475/ajs.301.45.455

Wobus, C., Whipple, K. X., Kirby, E., Snyder, N., Johnson, J., Spyropolou, K., et al. (2006). Tectonics from topography: Procedures, promise, and pitfalls. *Geological Society of America Special Papers*, *398*(4), 55–74. https://doi.org/10.1130/2006.2398(04)

Wobus, C. W., Hodges, K. V., & Whipple, K. X. (2003). Has focused denudation sustained active thrusting at the Himalayan topographic front? *Geology*, *31*(10), 861–864. https://doi.org/10.1130/G19730.1

Wobus, C. W., Whipple, K. X., & Hodges, K. V. (2006). Neotectonics of the central Nepalese Himalaya: Constraints from geomorphology, detrital $^{40}Ar/^{39}Ar$ thermochronology, and thermal modeling. *Tectonics*, *25*, TC4011. https://doi.org/10.1029/2005TC001935

Yanites, B. J., & Ehlers, T. A. (2012). Global climate and tectonic controls on the denudation of glaciated mountains. *Earth and Planetary Science Letters*, *325-326*, 63–75. https://doi.org/10.1016/j.epsl.2012.01.030

Yanites, B. J., & Ehlers, T. A. (2016). Intermittent glacial sliding velocities explain variations in long- timescale denudation, SW British Columbia. *Earth and Planetary Science Letters*, *450*, 52–61. https://doi.org/10.1016/j.epsl.2016.06.022

Yanites, B. J., & Tucker, G. E. (2010). Controls and limits on bedrock channel geometry. *Journal of Geophysical Research*, *115*, F04019. https://doi.org/10.1029/2009JF001601

Yanites, B. J., Tucker, G. E., Mueller, K. J., Chen, Y. G., Wilcox, T., Huang, S. Y., & Shi, K. W. (2010). Incision and channel morphology across active structures along the Peikang River, central Taiwan: Implications for the importance of channel width. *Bulletin of the Geological Society of America*, *122*(7–8), 1192–1208. https://doi.org/10.1130/B30035.1

Yue, L. F., Suppe, J., & Hung, J. H. (2005). Structural geology of a classic thrust belt earthquake: the 1999 Chi-Chi earthquake Taiwan (Mw = 7.6). *Journal of Structural Geology*, *27*(11), 2058–2083. https://doi.org/10.1016/j.jsg.2005.05.020

Ziesch, J., Tanner, D. C., & Krawczyk, C. M. (2014). Strain associated with the fault-parallel flow algorithm during kinematic fault displacement. *Mathematical Geosciences*, *46*(1), 59–73. https://doi.org/10.1007/s11004-013-9464-3